Chemical Engineering Journal xxx (xxxx) 154374

Contents lists available at ScienceDirect

Chemical Engineering Journal

journal homepage: www.elsevier.com/locate/cej

Precursor effect on the hydrothermal synthesis of pure ZnO nanostructures and enhanced photocatalytic performance for norfloxacin degradation

Ramon Resende Leite [a,*], Renata Colombo [b], Fausto Eduardo Bimbi Júnior [c], Marcos Roberto de Vasconcelos Lanza [c], Hernane da Silva Barud [d], Conrado Ramos Moreira Afonso [e], Maria Inês Basso Bernardi [a]

[a] São Carlos Institute of Physics, University of São Paulo, 13563-120 São Carlos, SP, Brazil
[b] School of Arts, Sciences and Humanities, University of São Paulo, 03828-000 São Paulo, SP, Brazil
[c] São Carlos Institute of Chemistry, University of São Paulo, 13560-970 São Carlos, SP, Brazil
[d] Biopolymers and Biomaterials Laboratory (BioPolMat), University of Araraquara, 14801-320 Araraquara, SP, Brazil
[e] Materials Engineering Department (DEMa), Federal University of São Carlos (UFSCar), 13565-905 São Carlos, SP, Brazil

ARTICLE INFO

Keywords:
One-step hydrothermal synthesis
Pure ZnO
Photocatalysis
Norfloxacin
Water remediation

ABSTRACT

The indiscriminate production and use of antibiotics have caused an environmental imbalance. Therefore, advanced oxidative processes such as photocatalysis have been proposed to eliminate the presence of such emerging pollutants. On the other hand, the use of photocatalytic processes requires the development of highly efficient photocatalysts. This paper introduces photocatalysts based on ZnO nanostructures with different morphologies and grown by low-temperature hydrothermal synthesis. The choice of zinc precursor resulted in significant variations in both the morphology and size of the ZnO particles. Morphologies, such as, dumbbell-like structures, nanogranules, and ellipsoidal particles were obtained by altering the zinc precursor in a slightly alkaline medium, and parameters such as photocatalyst dosage, initial concentration of antibiotic Norfloxacin (NOR), and pH in photocatalysis were thoroughly investigated. The reactive species responsible for NOR degradation were photogenerated holes, superoxide radicals, and hydroxyl radicals, with the latter showing a greater contribution. Degradation pathways are also proposed, and intermediate products were identified by LC-MS. Thirteen degradation products, of which six were reported for the first time, were detected. Among the synthesized morphologies, nanogranules exhibited superior photocatalytic activity, achieving 100% NOR degradation after 70 min under UV-C light and excellent reusability after three cycles (97%). The results surpass those from previous studies, since the simple and efficient photocatalysts employed led to shorter degradation times.

1. Introduction

The growth of the global population, coupled with increasing demands for water for agricultural, industrial, and domestic purposes, has compromised water quality [1]. The supply of clean and affordable water to communities is a global challenge due to the degradation of water resources [2]. Covering approximately 70 % of the Earth's surface, water stands as one of the most plentiful natural resources [3]; however, only 1.1 % is available and safe for human consumption [4]. In 2022, the Joint Monitoring Programme for Water Supply, Sanitation, and Hygiene (JMP), conducted by the World Health Organization (WHO) and the United Nations Children's Fund (UNICEF), presented alarming findings regarding global inequities. Unbelievably, 2.2 billion people lacked access to clean drinking water, 3.5 billion to proper sanitation, and 2 billion to even the most basic handwashing facilities [5].

The significant concentrations of pharmaceutical compounds, especially antibiotics, in water bodies have been recently reported as a challenge in the field of environmental remediation [6] due to the increasing bacterial resistance to antibiotics and the limitations of conventional water treatments for removing certain contaminants to safe levels for human consumption [7,8]. Among the pharmaceutical products commonly found in water resources, compounds belonging to the class of fluoroquinolones (FQs) are emerging pollutants of serious global concern [9]. FQs are among the most consumed antibiotics, totaling approximately 44 million kilograms per year [10], and are widely used in treatments of bacterial infections in humans and animals [11]. Typical representatives of such compounds include norfloxacin (NOR),

* Corresponding author.
E-mail address: ramon.rleite@usp.br (R. Resende Leite).

https://doi.org/10.1016/j.cej.2024.154374
Received 25 March 2024; Received in revised form 23 July 2024; Accepted 27 July 2024
1385-8947/

ciprofloxacin (CIP), enrofloxacin (ENR), ofloxacin (OFX), and lomefloxacin (LOM) [12]. High concentrations of FQs, including NOR (703 $\mu g \cdot L^{-1}$), CIP (185 $\mu g \cdot L^{-1}$), and LOM (159 $\mu g \cdot L^{-1}$), have been detected in effluents from pharmaceutical and hospital waste treatments [9].

Traditional wastewater treatment plants are ineffective at degrading FQs [9]. Although different methods for removing those contaminants have been evaluated, most conventional technologies, including biological, chemical, and adsorption processes, are not designed to address/degrade pharmaceutical compound residues during treatments [7,13]. Due to the antibacterial properties of antibiotics, biological methods are not efficient in promoting degradation and, besides, are time-consuming [14]. The adsorption process only transfers the contaminants from the liquid phase to the solid phase without modifying their toxic characteristics [15,16]. Therefore, viable, environmentally friendly, sustainable, and cost-effective technologies must be developed for the effective degradation of those contaminants [17].

Advanced Oxidation Processes (AOP) have been increasingly recognized as effective physicochemical treatment methods and have aroused interest for their ability to eliminate persistent organic compounds, including pharmaceuticals. They generate highly reactive hydroxyl radicals, exhibiting non-selectivity towards both organic and inorganic compounds [18,19], and their use results in the conversion and breakdown of persistent organic compounds, producing biodegradable organic byproducts and mineralizable compounds that pose minimal toxicity to ecosystems [20]. Among AOPs, heterogeneous photocatalysis is a promising method due to its high efficiency, low cost, simple design, moderate reaction conditions, environmental friendliness, high mineralization rate, and applicability for degrading a variety of organic pollutants, even at low concentrations [21].

Photocatalysis has been considered one of the best methods for the removal or photodegradation of pharmaceutical products in water since it requires only the use of light and photocatalysts, thus being energy-efficient [22]. A material selected for use as a photocatalyst should be inexpensive, non-toxic, easily processable, and, above all, efficient. Semiconductor metal oxides have been regarded as promising materials for acting as photocatalysts in wastewater treatment processes. Among them, ZnO has been widely used for the degradation of FQs due to its high photocatalytic activity, low cost, adjustable morphology, and non-toxicity [23,24]. Topkaya et al. (2014) investigated the use of pure ZnO plates in the degradation of ENR under UV light and achieved approximately 75 to 78 % efficiencies after 120 min [25]. In the study by Chen et al. (2021), the magnetic flake ZnO/g-C_3N_4 photocatalyst exhibited outstanding efficacy in eliminating NOR, achieving a degradation exceeding 90 % after 120 min [26]. More recently, Batterjee et al. (2022) employed spherical ZnO nanoparticles for the photocatalytic degradation of CIP under UV light, reaching 82 % efficiency in 160 min [27]. Makota et al. (2024) developed a sphere-shaped ZnO photocatalyst, which demonstrated complete degradation of OFX after 210 min of photocatalytic reaction under UV light [24]. For the degradation of NOR under UV light, ZnO photocatalysts based on heterojunctions and nanocomposites with other materials have been proposed to achieve high photocatalytic activity [28,29]. However, long degradation times are required, thus compromising the practical applications of those photocatalysts. To the best of our knowledge, research on the use of pure ZnO nanostructures for the effective and rapid degradation of NOR under UV-C light has not been well documented.

This paper reports on a facile synthesis of dumbbell-like, nanogranules and ellipsoidal ZnO particles by a hydrothermal process that alters the zinc precursor. The possible mechanisms for the formation of such structures are discussed in detail. The materials obtained were used as photocatalysts for the degradation of norfloxacin under UV-C light, and the effects of the dosage of the three ZnO photocatalysts (0.25 – 1.0 $g \cdot L^{-1}$), initial concentration of the contaminant (5 – 10 $mg \cdot L^{-1}$), and pH of the NOR solution (6 – 10) were thoroughly investigated. A degradation mechanism is proposed, and the main oxidative species, products, and degradation pathways were identified for the most effective photocatalyst. Among the synthesized morphologies, nanogranules exhibited the highest photocatalytic activity, achieving complete degradation of NOR within 70 min. The high photocatalytic activity of ZnO nanogranules demonstrated offers promising prospects for real-world applications in the fields of advanced water treatment and emergent pollutant degradation.

2. Experimental

2.1. Chemicals

This section is provided in the Supplementary Information (S1).

2.2. Synthesis of ZnO nanostructures

Aqueous solutions of 0.05 M were prepared from the dissolution of different precursors, such as zinc acetate dihydrate, zinc chloride, and zinc nitrate hexahydrate, in double-distilled water. Under constant agitation, the pH of the solutions was adjusted to 8 by a dropwise addition of a 0.5 M NaOH solution. The resulting suspensions were then transferred to individual autoclavable laboratory flasks, and hydrothermal treatments were applied at 110 °C for 4 h. After completion of the reaction, a white precipitate was obtained, washed repeatedly with ethanol and distilled water, and finally dried at 80 °C. The samples were called ZnO-X, where X (X: A-acetate, Cl-chloride, or N-nitrate) specifies the precursor used.

2.3. Characterization techniques

The crystal structure of the synthesized materials was characterized by XRD (Rigaku Ultima IV, Japan) using CuK_α. The morphologies were characterized under a field-emission scanning electron microscope (FE-SEM SUPRA™35, Carl Zeiss, Germany) operating at 5 kV, and transmission electron microscopy (TEM) analysis was performed on an FEI Tecnai G2 F20 200 kV equipped with a field emission gun (FEG). The optical property was identified in a UV–Vis spectrophotometer (Shimadzu UV-2600i, Japan), and the surface area was determined by N_2 adsorption–desorption analysis at 77 K by a Micrometrics ASAP 2020 model instrument (EUA). Photoluminescence spectra were obtained at room temperature using a Jobin Yvon Horiba Fluorolog Spectrofluorometer model FL3-221 with an excitation wavelength of 325 nm. A 370 nm filter was used to filter the stray light.

Electrochemical impedance spectroscopy (EIS) and transient photocurrent analysis were conducted on synthesized ZnO samples using a three-electrode setup under UV-C lamp irradiation (8 W). The setup consisted of an Ag/AgCl reference electrode (3 M KCl), a Pt counter electrode, and a glassy carbon electrode (Metrohm Autolab PGSTAT302N). The electrolyte used was 0.1 $mol \cdot L^{-1}$ K_2SO_4 under N_2(g) saturation in the open circuit potential (OCP) region. For these tests, 2 mg of the photocatalyst was weighed and dispersed in 1 mL of 70 % (v/v) ethylic alcohol using ultrasound, and then 15 μL of this ink was dropped onto the glassy carbon surface (A = 0.2475 cm^2), obtaining a loading of 0.121 $mg \cdot cm^{-2}$.

2.4. Photocatalytic activity test and analysis

The photocatalytic performance of the samples was evaluated for NOR degradation under UV-C light irradiation (six lamps of 15 W OSRAM Germicidal, λ = 254 nm). An amount of ZnO photocatalyst was dispersed in 50 mL of a NOR aqueous solution, and the effects of the experimental parameters, e.g., photocatalyst loading (12.5 – 50 mg), NOR concentration (5 – 10 $mg \cdot L^{-1}$), and initial pH of the NOR solution (6 – 10, adjusted by 0.1 mol/L HCl and 0.1 mol/L NaOH) on the NOR pho-

todegradation were investigated. Prior to irradiation, the suspension was stirred in the dark for 60 min for the development of adsorption–desorption equilibrium. The experiment was then conducted at intervals of 10 or 20 min and the UV–Vis absorption spectrum was recorded. The absorption maxima value of NOR at 273 nm was used for the monitoring of the photocatalytic performance of ZnO NPs in a UV–Vis spectrophotometer (Kasuaki IL-593).

The intermediate products of NOR photodegradation were identified by liquid chromatography tandem mass spectrometry (LC-MS/MS) on an LC/MS-8030 triple quadrupole (Shimadzu Co., Japan). Separation occurred on a Shim-pack ODS II column (3 mm i.d. × 100 mm, 2.2 μm) at 26 °C. The mobile phase comprised water (A) and acetonitrile (B), both containing 0.1 % formic acid, and elution was executed at a 0.8 $mL{\cdot}min^{-1}$ flow rate with the following gradient program: 0–5 min: 10–37 % (B); 5–8 min: 37–100 % B; and 8–10 min: 100–10 % B. The electrospray interface (ESI) operated in positive ionization mode at 400 °C and 4.5 kV, and full-scan spectra were acquired in positive ion mode across a 100 to 500 *m/z* range. Nitrogen was employed as both a nebulizer and a desolvation gas at 3 and 15 $L{\cdot}min^{-1}$ flowing rates, respectively.

The role of reactive species involved in the photocatalytic degradation of NOR was investigated in radical-trapping experiments. Tert-butanol (t-BuOH), ammonium oxalate (AO), ascorbic acid (AA), and silver nitrate ($AgNO_3$) were used as scavengers of •OH, h^+, $•O_2^-$, and e^-, respectively. The methodology adopted is described in Lima et al. (2021) [30].

To identify the main working oxidant species, electron paramagnetic resonance (EPR) tests were also carried out using DMPO (5,5-dimethyl-1-pyrroline N-oxide) as spin probes to confirm the presence of radicals. The EPR measurements were performed in an E-109 X-band Varian system spectrometer, equipment with a standard rectangular cavity, and aliquots of the samples of 200 μL were transferred into an EPR glass quartz flat cell. A reference signal for the EPR intensity and magnetic field calibration has been obtained using Cr^{III} (g = 1.9797) as an impurity in the MgO crystal. Measurement conditions were: CenterField = 340 mT, SweepWidth = 12 mT, SweepTime = 60 s, Number of Points = 1024, MW Power = 20 mW, Gain = 1.0, ModField = 0.1 mT, ModFreq = 100 kHz, Time Const = 0.064 s, MW Freq = 9.5006 GHz. Spectral simulations were done using an Easyspin program.

Under optimized conditions, the same photocatalyst was subjected to three consecutive usage cycles. At each cycle, the photocatalyst was collected, repeatedly washed with distilled water, and dried at 100 °C.

3. Results and discussion

3.1. Characterizations

Fig. 1 shows the XRD patterns of the samples produced from different zinc salt precursors. All diffraction peaks can be indexed to a hexagonal wurtzite structure of ZnO (JCPDS No. 36–1451). No other crystalline phases or impurities were detected. The Scherrer equation calculated the crystalline size [31], leading to 19 nm, 23 nm, and 37 nm values for ZnO-Cl, ZnO-N, and ZnO-A samples, respectively. Crystalline size depends on the counterions (CH_3COO^-, Cl^-, or NO_3^-) present in the zinc precursor [32]. The smaller size observed in the chloride-generated sample may be attributed to the reduced growth rate of wurtzite during the hydrothermal process.

The morphology of ZnO prepared from various precursors was investigated by the SEM technique. As shown in Fig. 2(a–f), a ZnO dumbbell-like, nanogranule and ellipsoidal morphology were obtained when acetate, chloride, and nitrate precursors, respectively, were used. The dumbbell-like ZnO consists of two twinned hexagonal prism shapes whose diameters ranged between 500 and 600 nm and lengths varied from 1.2 to 1.6 μm (Fig. 2a–b). ZnO nanogranules were characterized

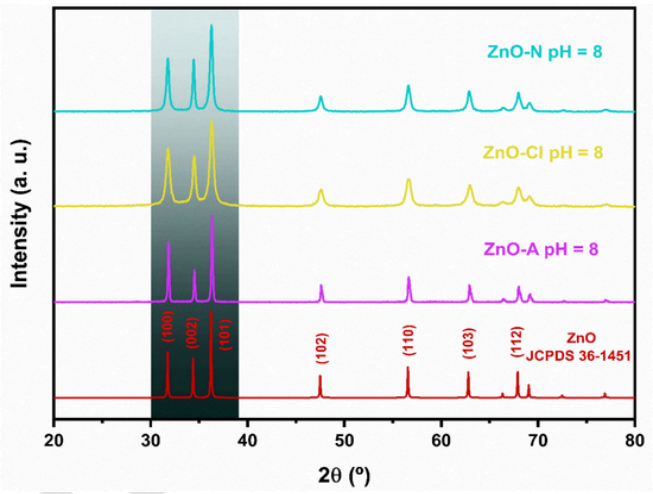

Fig.1. XRD patterns of ZnO-A, ZnO-Cl, and ZnO-N prepared via the hydrothermal route.

by globular particles of less than 40 nm diameter (Fig. 2c–d). On the other hand, the ellipsoidal structure has a 1 μm average length and ~400 nm diameter (Fig. 2e–f).

TEM analysis was further conducted to obtain information about the size and morphology of the synthesized ZnO particles. Fig. 3(a–b) shows TEM images in bright field (BF) mode of ZnO nanogranules at different magnifications. From these BF TEM images, the average particle size was estimated to be about 40 nm, consistent with estimates obtained by SEM. The crystalline structure was further investigated using advanced techniques such as selected area electron diffraction (SAED) and high-resolution transmission electron microscopy (HRTEM). A ring SAED pattern confirmed the polycrystalline nature of the ZnO nanogranules [33], with diffraction rings corresponding to the crystallographic planes (1 0 0), (0 0 2), (1 0 1), and (1 0 2) of the wurtzite structure of ZnO [34]. The interplanar distance for the nanogranules was calculated to be approximately 0.25 nm, corresponding to the (1 0 1) plane, using HRTEM images (Fig. 3c). Fig. 3 (d–e) shows low- and high-magnification images of ZnO ellipsoidal shapes. These ellipsoidal shapes consist of elongated submicrometer-sized particles with an average diameter of about 400 nm, as previously investigated by SEM. However, the SAED pattern observed for the ellipsoids is less defined compared to that of the ZnO nanogranules. Larger particles may scatter electrons more diffusely, resulting in less sharp SAED patterns, as observed. The lattice fringe spacing for the ZnO ellipsoids was found to be approximately 0.19 nm, corresponding to the (1 0 2) diffraction plane of ZnO [35], as illustrated in Fig. 3f.

The difference in ZnO morphology can be attributed to the influence of counterions [36], whose adsorption on the growth direction of particles is significantly influenced by the chemical interactions between the ions and the particles [32]. ZnO exhibits a dumbbell-like structure due to twinning along the (0001) plane, with each crystallite growing along the $[000\bar{1}]$ direction on both sides of the twinning plane [37]. The individual crystallite in the twin crystal grew along the polar c-axis, where CH_3COO^- may intercalate between the polar Zn (0001) faces of two individual rod crystals to form the dumbbell-like shape [38,39].

In hydrothermal synthesis with no use of additives, such as, surfactants, Cl^- ions are strongly adsorbed onto the positively charged surface (0001) [40], and their electrostatic adsorption inhibits growth along the basal plane (0001), thus reducing the polar surface charge density [41,42]. Consequently, the intrinsically anisotropic growth of ZnO along the (0001) facet is suppressed, so that the lateral growth rate is considerably greater than the one along the c-axis direction, and nanogranules are formed. Furthermore, synthesis with a chloride pre-

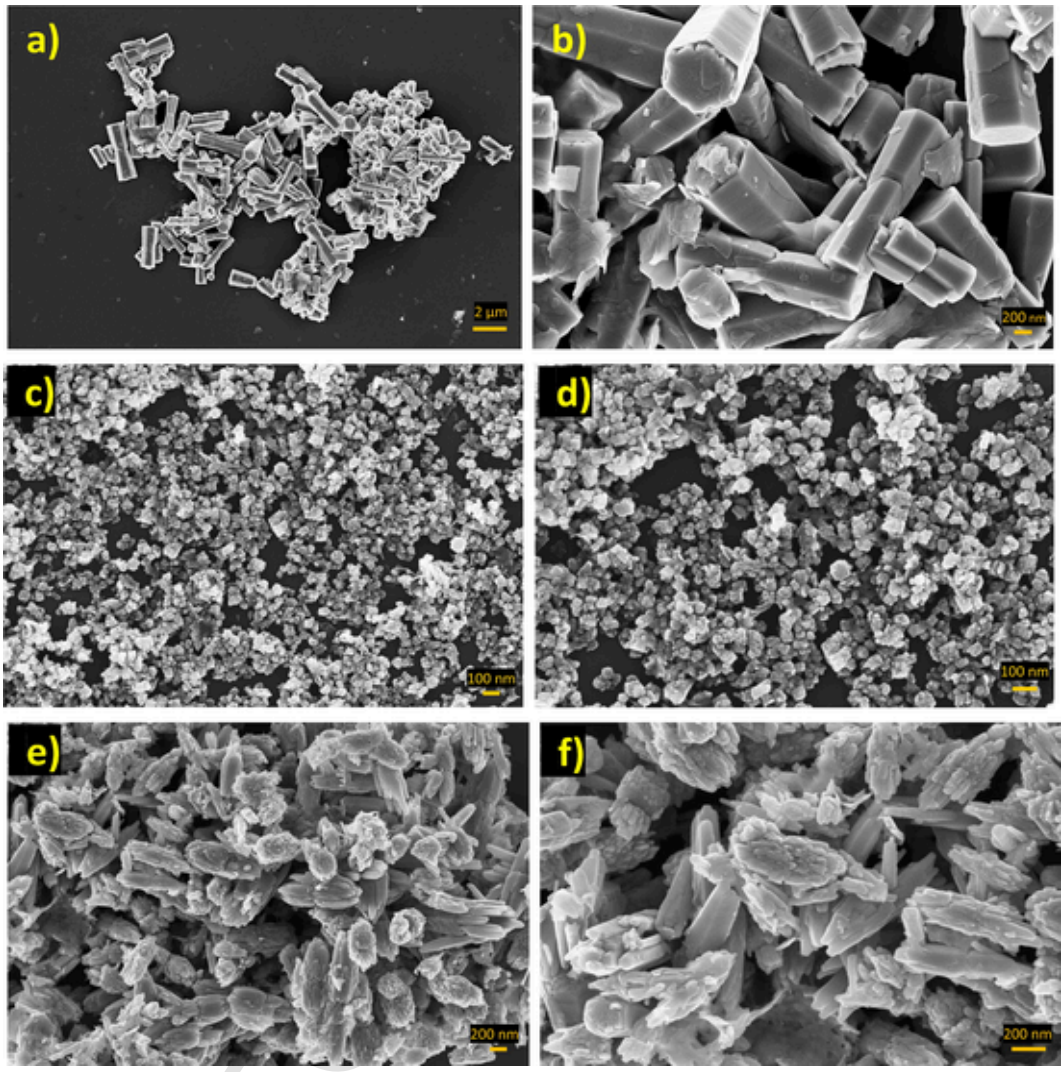

Fig.2. FESEM images of (a, b) ZnO-A, (c, d) ZnO-Cl (e, f), and ZnO-N.

cursor resulted in particles of smaller dimensions since chloride has a stronger interaction with surfaces compared to acetate and nitrate ions [43]. As a result, the more intense adsorption of chloride on the surface limits the growth of ZnO particles, leading to smaller particle sizes compared to syntheses that use acetate or nitrate as precursors.

Nitrate anion tends to act as a non-coordinating ligand in the formation of the hexagonal wurtzite crystal structure [43], i.e., it has no strong interaction with metal ions, such as Zn^{2+}, facilitating the preferential growth orientation of particles with an elongated, ellipsoid-like shape of ZnO towards the c-axis (plane 0001). According to the microstructure shown in Fig. 2e–f, it appears the ellipsoidal-shaped ZnO particles do not consist of a single crystal but are made up of smaller particles. It is evident that smaller particles serve as building blocks for forming such a morphology [44]. The ellipsoids formed through the germination of a second half at the base of a half-ellipsoid [45], suggesting ellipsoidal nanostructures are self-assembled by primary nanoparticles by the oriented-attachment mechanism [46].

The optical properties of ZnO nanostructures, obtained through the hydrothermal route, were investigated by UV–Vis spectroscopy. As illustrated in Fig. 4a, the spectra show intense absorption at wavelengths below 400 nm for all analyzed samples. The maximum absorption peaks were recorded at 389 nm, 373 nm, and 382 nm for ZnO-A, ZnO-Cl, and ZnO-N, respectively, characterizing the electronic transition from the valence band to the conduction one (O 2p → Zn 3d) in the wurtzite structure of ZnO [47]. Additionally, low absorption occurs between 400 nm and 800 nm, which highlights the predominance of absorption in the ultraviolet region and high transparency in the visible range [48,49]. A blue shift in the excitonic absorption edge is observed in all spectra, compared to bulk ZnO ($\lambda = 368$ nm) [50]. The blue shift in the absorption edge is associated with a reduction in the ZnO particle size, a phenomenon attributed to the Moss-Burstein effect [51,52].

Band gap energy (E_g) is crucial in photocatalytic reactions since it determines the minimum energy required to activate the photocatalyst [47]. The E_g of the prepared samples was estimated by the Tauc equation and considering ZnO as a direct bandgap semiconductor [53]:

$$(\alpha h\nu)^2 = A(h\nu - E_g) \quad (1)$$

where α is the absorption coefficient, $h\nu$ is the photon energy, A is a constant, and E_g is the direct band gap energy. The extrapolation of the linear portion of the $(\alpha h\nu)^2$ versus photon energy ($h\nu$) graph to $(\alpha h\nu)^2 = 0$ was performed for the determination of E_g [54]. The band gap energies for ZnO-A, ZnO-Cl, and ZnO-N were 3.19, 3.32, and 3.24 eV, respectively (Fig. 4b). ZnO-Cl shows the highest E_g value due to its smaller particle size compared to the other two samples. Additionally, in comparison to bulk ZnO (with $E_g = 3.37$ eV), a reduction in E_g

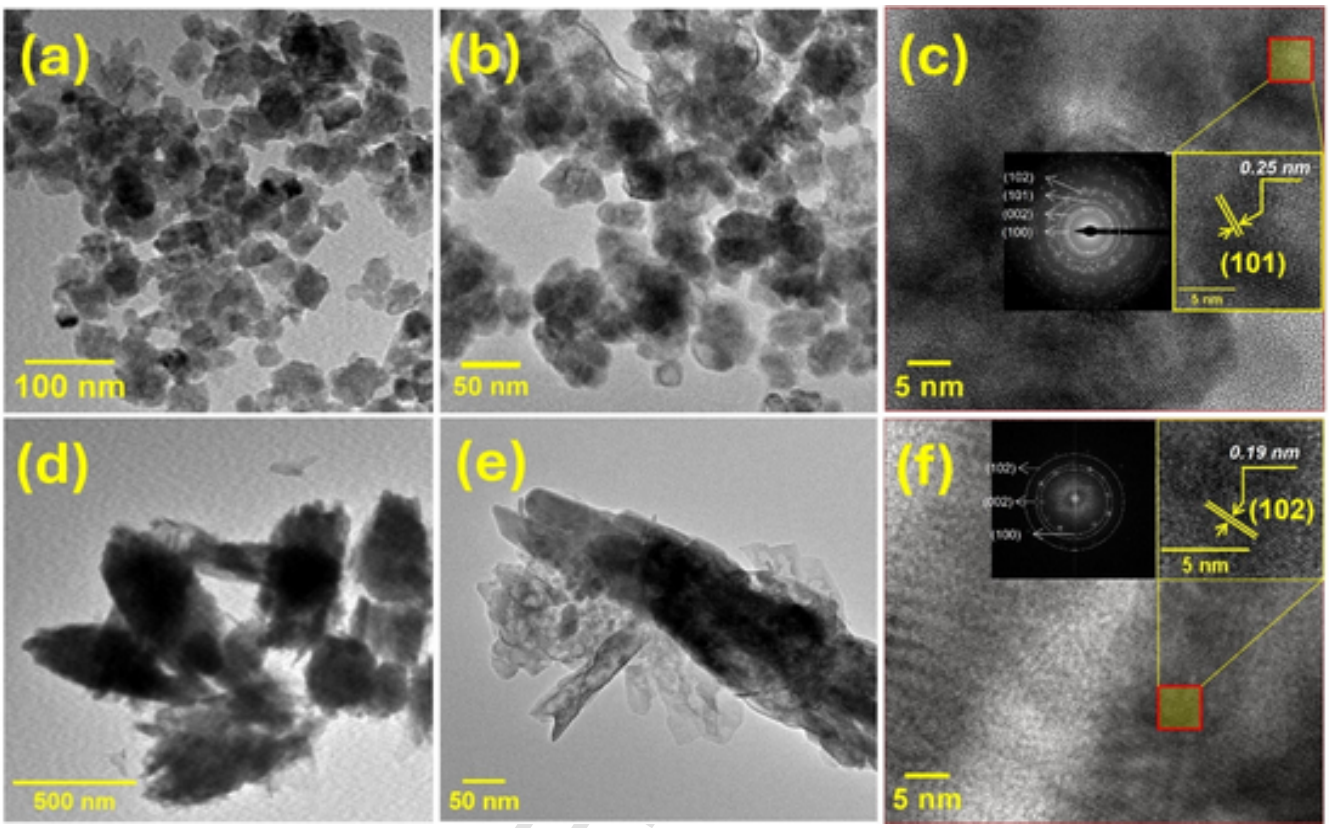

Fig.3. TEM images of ZnO samples: (a, b) low- and high-magnification views of nanogranules, with corresponding (c) HRTEM image and SAED pattern. (d, e) Low- and high-magnification views of ellipsoidal ZnO particles, accompanied by (f) HRTEM image and SAED pattern.

was observed in the synthesized ZnO nanostructures and attributed to the effects of quantum confinement and the formation of intrinsic crystalline defects [55].

It is well known that surface area significantly affects the photocatalytic performance of ZnO. A large one is favorable for effective contact between the pollutant and the photocatalyst surface [56] and provides more active sites for photocatalytic reactions. According to the IUPAC classification, the N_2 adsorption–desorption isotherms of all samples exhibit typical Type IV isotherms with H3 hysteresis loops, suggesting the presence of mesoporous structures (Fig. 4c) [57]. The BET surface areas of ZnO-A, ZnO-Cl, and ZnO-N, calculated from N_2 adsorption and desorption isotherms, were approximately 7, 41, and 16 m^2/g, respectively (Fig. 4d). The greater surface area of ZnO-Cl is associated with its smaller particle size compared to ZnO-A and ZnO-N.

The elemental composition and valence state of ZnO photocatalysts were investigated by XPS. As shown in Fig. 5a–c, the survey spectra of the ZnO nanostructures identified the presence of three chemical elements, namely, C 1s, Zn 2p, and O 1s, of which carbon can be attributed to adventitious carbon [31]. The high-resolution XPS spectra of Zn 2p shown in Fig. 5(d–f) exhibited symmetric peaks at binding energies of ~1022.1 and ~1045.2 eV, corresponding to Zn $2p_{3/2}$ and Zn $2p_{1/2}$ orbitals, respectively [58]. The spin–orbit splitting of 23.1 eV between Zn $2p_{3/2}$ and Zn $2p_{1/2}$ suggests Zn species in the wurtzite structure are in the divalent (2 +) valence state [59], and the high-resolution O 1s spectra shown in Fig. 5(g–i) were deconvoluted into three peaks fitted to a Gaussian-Lorentzian function. The peak at the lowest binding energy, O_L, centered around 530.3 eV, is attributed to O^{2-} ions involved in the Zn-O bonding of the wurtzite structure of the hexagonal arrangement of ZnO [60]. At intermediate binding energy, the peak centered in the 531.3 to 531.8 eV range corresponds to Zn-OH bonding of hydroxyl groups adsorbed on the surface of the photocatalysts [61]. Furthermore, at higher binding energies, the peak ranges between 532.5 and 533.1 eV corresponds to adsorbed H_2O molecules [61] and the C–O bonding of adventitious carbon [62].

It is widely recognized that the presence of OH groups on the surface of photocatalysts plays a crucial role in photocatalytic processes [63]. Hydroxyl groups present on such a surface can act as traps for photogenerated holes, capturing them and forming hydroxyl radicals (•OH). It also helps suppress the recombination of the electron-hole pair, which is crucial for maintaining high photocatalytic efficiency since recombination would decrease the availability of active charge carriers for participating in oxidation reactions in the degradation of organic pollutants [36]. Therefore, a semi-quantitative analysis of those groups was conducted in each sample and calculated the relative ratio between the integration areas of the peaks attributed to OH groups by oxygen from the lattice in the XPS O 1 s spectra. The ratios of $\frac{\int O_{OH}}{\int A_{O_L}}$ for ZnO-A, ZnO-Cl, and ZnO-N at pH = 8 were 8.5, 14.6, and 9.4, respectively. The higher concentration of hydroxyl groups in ZnO-Cl at pH = 8 was beneficial for increasing the photocatalytic efficiency in NOR degradation. Additionally, the relative ratio between the integration areas of adsorbed water species and adventitious carbon bondings by lattice oxygen was calculated. The ratios of $\frac{\int A_{O_{H_2O/C-O}}}{\int A_{O_L}}$ for the aforementioned samples were 6.7, 17.7, and 9.0, respectively, suggesting higher surface reactivity of the nanogranular ZnO photocatalyst, i.e., for ZnO-Cl at pH = 8. The higher surface reactivity of ZnO nanogranules can be attributed to the larger surface area presented (41 m^2/g).

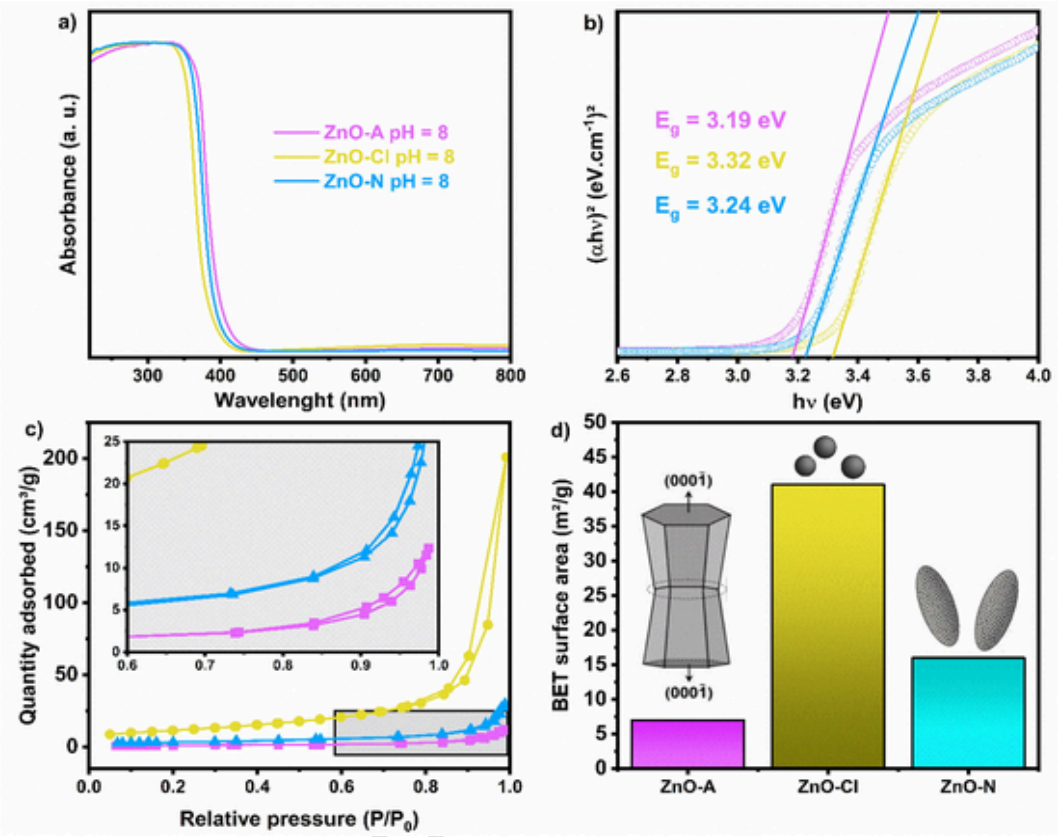

Fig.4. (a) UV–vis absorption, (b) estimation of the band gap by Tauc plot, (c) N_2 gas adsorption–desorption isotherms curves, and (d) BET surface area of ZnO-A, ZnO-Cl, and ZnO-N pH = 8.

3.2. Investigation of factors that influence the photocatalytic degradation of NOR

Degradation experiments of the drug NOR under UV-C light investigated the photocatalytic performance of the synthesized ZnO nanostructures, and factors such as photocatalyst dosage, initial NOR concentration, and photocatalysis pH were meticulously studied.

3.2.1. Effect of ZnO dosage as a photocatalyst

Evaluations of catalytic dosage are crucial in the degradation of emerging pollutants since they directly affect the removal of pharmaceutical products and the costs involved [27,64]. The effect of ZnO dosage on the degradation of NOR (10 mg·L^{-1}) was investigated, and the result is shown in Fig. 6. According to the Fig. 6a, when the ZnO-A dosages were 0.25, 0.5, and 1.0 g·L^{-1}, the NOR removal rates were 81, 83.2, and 87.5 % in 180 min of reaction, respectively. However, in terms of photocatalytic performance, the increase in ZnO-A concentration exerted no significant influence at the end of the evaluated reaction time (Fig. 6b). Such a result may be attributed to the larger particle size and small surface area, which contributed to the saturation of active sites and the limited diffusion of reactive species responsible for the photocatalytic activity. The increase in ZnO-A photocatalyst concentration did not lead to a proportional improvement in the NOR degradation rate, as evidenced by the constancy of "*k*" around 0.00774 min^{-1} (Fig. 6c). Therefore, the optimal dosage of ZnO-A is 0.25 g·L^{-1}.

After 70-minute exposure to UV-C light, an increase in the dosage of ZnO-Cl from 0.25 to 1.0 g·L^{-1} improved the photocatalytic degradation rate from 89.7 to 100 % (Fig. 6d–e). The increased amount of photocatalyst promoted a higher generation of reactive oxidation species (ROS) responsible for the degradation of NOR [28]. Due to its high surface area, the increased dosage of ZnO-Cl was beneficial for photocatalytic performance because of the greater availability of active sites on the catalyst's surface [65]. The 1.0 g·L^{-1} concentration resulted in greater adsorption of the NOR molecule on the photocatalyst's surface, favoring its degradation. The kinetic constant varied from 0.03313 to 0.07279 min^{-1} when the concentration of ZnO-Cl was increased from 0.25 to 1.0 g·L^{-1} (Fig. 6f). In comparison to the other photocatalysts studied, nanogranules exhibited a higher kinetic constant, reflecting not only improved efficiency but also reduced photodegradation times. The higher specific surface area and mesoporous structures present in ZnO-Cl pH = 8 (nanogranules) contributed to its high adsorption capacity and efficiency in the photodegradation of NOR. The increase in surface area provides more active sites for the generation of radicals, and, consequently for improving the photocatalytic process [66].

Fig. 6g shows that an increase in the catalyst dosage in ZnO-N also led to higher NOR removal efficiency. When the ZnO-N dosages were 0.25, 0.5, and 1.0 g·L^{-1}, the NOR removal rates were 89.3, 95.2, and 98.9 % in 180 min, respectively. The increase in ZnO-N dosage in an aqueous medium containing the contaminant resulted in a corresponding increase in degradation efficiency and kinetic constant. The respective efficiencies of photocatalytic degradation of that drug were 82.0, 90.6, and 97.7 % (Fig. 6h). As observed for ZnO-Cl, "*k*" proved sensitive to the amount of photocatalyst used (Fig. 6i).

A fixed concentration of 0.25 g·L^{-1} of ZnO-N and ZnO-Cl photocatalysts was chosen for the subsequent experiments for minimizing costs and for comparative purposes with ZnO-A.

3.2.2. Effect of initial NOR concentration

The antibiotic concentration in the wastewater system also acts as a key parameter in optimizing the photocatalytic degradation process

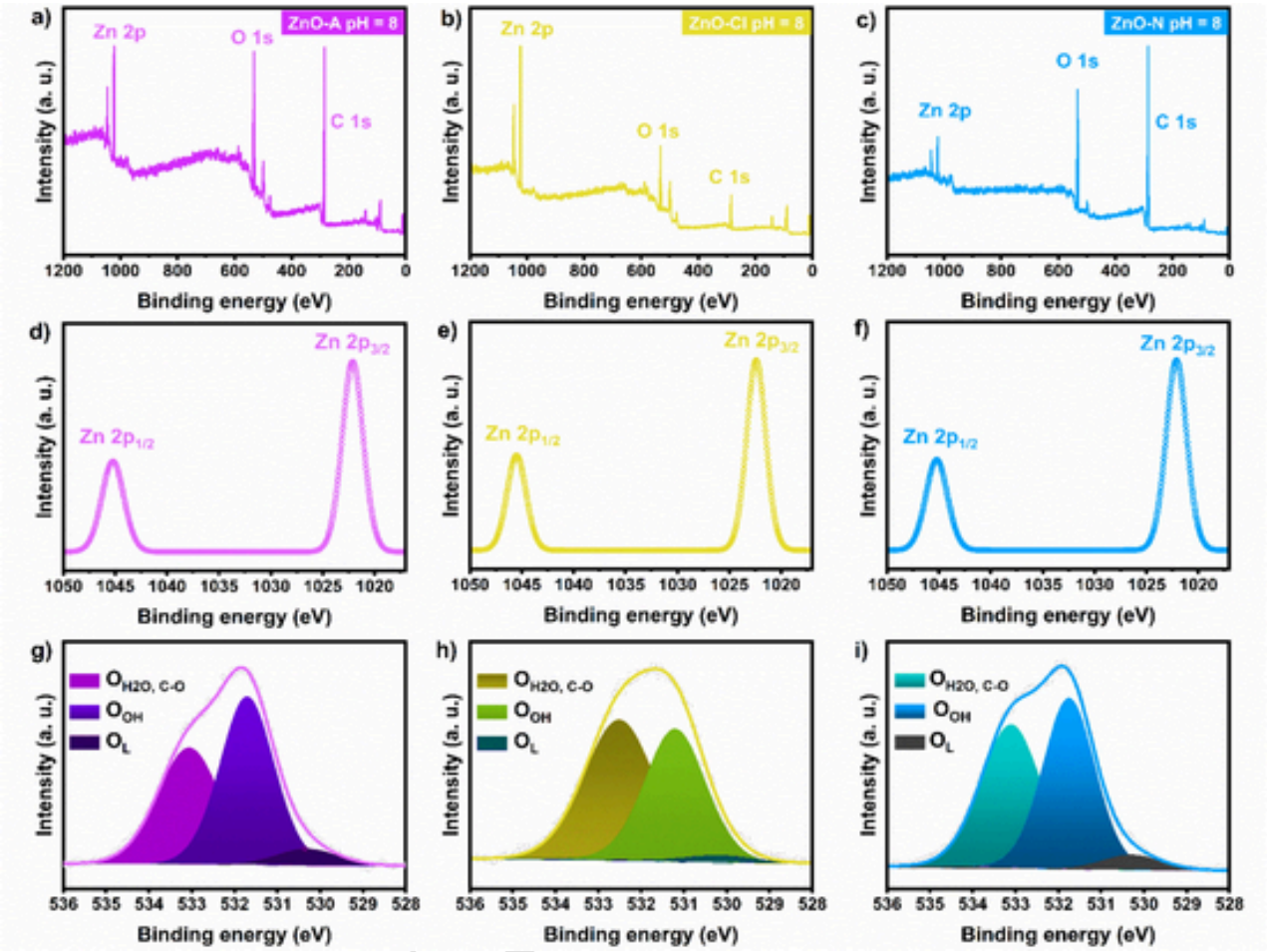

Fig.5. XPS spectra of ZnO nanostructure samples: (a, b, c) survey, (d, e, f) Zn 2p, and (g, h, i) O 1s.

[67]. In a natural environment, the concentration of compounds belonging to the class of FQs such as NOR substantially varies [9], which requires analyses of the impact of various initial NOR concentrations on the photocatalytic performance. The influence of the initial NOR solution concentration (5 – 10 mg·L^{-1}) was investigated, and the results for ZnO-A, ZnO-Cl, and ZnO-N are summarized in Fig. 7. The reaction conditions were 0.25 g·L^{-1} photocatalyst dosage and pH = 8.

A higher adsorption of the drug on the photocatalyst surfaces was observed as the initial NOR concentration increased (Fig. 7a, d, and e). After 180-minute UV-C light exposure, the photocatalytic efficiencies of ZnO-A were 74.9, 71.1, and 68.01 % for initial NOR concentrations of 5, 7.5, and 10 mg·L^{-1}, respectively (Fig. 7b). A decrease in k from 0.01025 to 0.00703 min^{-1} was observed as the NOR concentration increased (Fig. 7c). ZnO-Cl exhibited the highest photoactivity among the samples, with complete degradation of the contaminant in a shorter exposure time to UV-C light. After a 70-minute photocatalytic treatment with ZnO-Cl and 5 mg·L^{-1} of NOR, no maximum absorption peak centered at 273 nm was observed, suggesting complete degradation of the quinolone ring. The increase in concentrations to 7.5 and 10 mg·L^{-1} resulted in a slight decrease in performance of 99.4 and 93.4 %, respectively (Fig. 6e). Higher kinetic constants were also detected in ZnO-Cl, highlighting its potential as a photocatalyst for degrading NOR under UV-C light exposure (Fig. 7f).

As shown in Fig. 7h, the NOR degradation rate for ZnO-N reached the maximum degradation for the lowest pollutant concentration, with 94.9 % efficiency after 180 min. An increase in the initial antibiotic concentration to 10 mg·L^{-1} led to a 13 % decrease in photocatalytic activity for the ZnO-N catalyst. Regarding kinetics, the value of k for ZnO-N decreased from 0.02177 to 0.00991 min^{-1} with the increase in the initial NOR concentration in the evaluated range (Fig. 7i).

In general terms, an increase in the initial concentration of NOR results in a decrease in the degradation rate [68]. Degradation efficiency decreases due to three synergistic factors. Firstly, for a fixed amount of photocatalyst, an increase in the NOR concentration leads to a greater occupation of active sites on the photocatalyst's surface by both NOR molecules and their intermediates, reducing the generation of ROS [65]. A higher NOR concentration produces a higher concentration of antibiotic intermediate products that compete with NOR molecules for active sites [69,70,71]. Secondly, at higher NOR concentrations, the reaction rate is limited by the amount of free radicals generated in the reaction mixture [65]. Lastly, when a higher NOR concentration is used, a significant amount of light can be absorbed by NOR molecules in the solution rather than the photocatalyst [16], which restricts the penetration of light into the aqueous solution, hampering the absorption of light by the catalyst and reducing the production of free radicals [65, 72]. According to Patel et al. (2020) [64], the developed photocatalysts showed high degradation efficiency at low initial concentrations of NOR. Therefore, the optimal initial concentration of NOR was 5 mg·L^{-1} for the subsequent experiments, corresponding to the condition of maximum degradation efficiency.

3.2.3. *Influence of the initial pH of the NOR solution*

The evaluation of pH is crucial since it impacts both the pollutant adsorption capacity and the efficiency of photodegradation [30]. Pho-

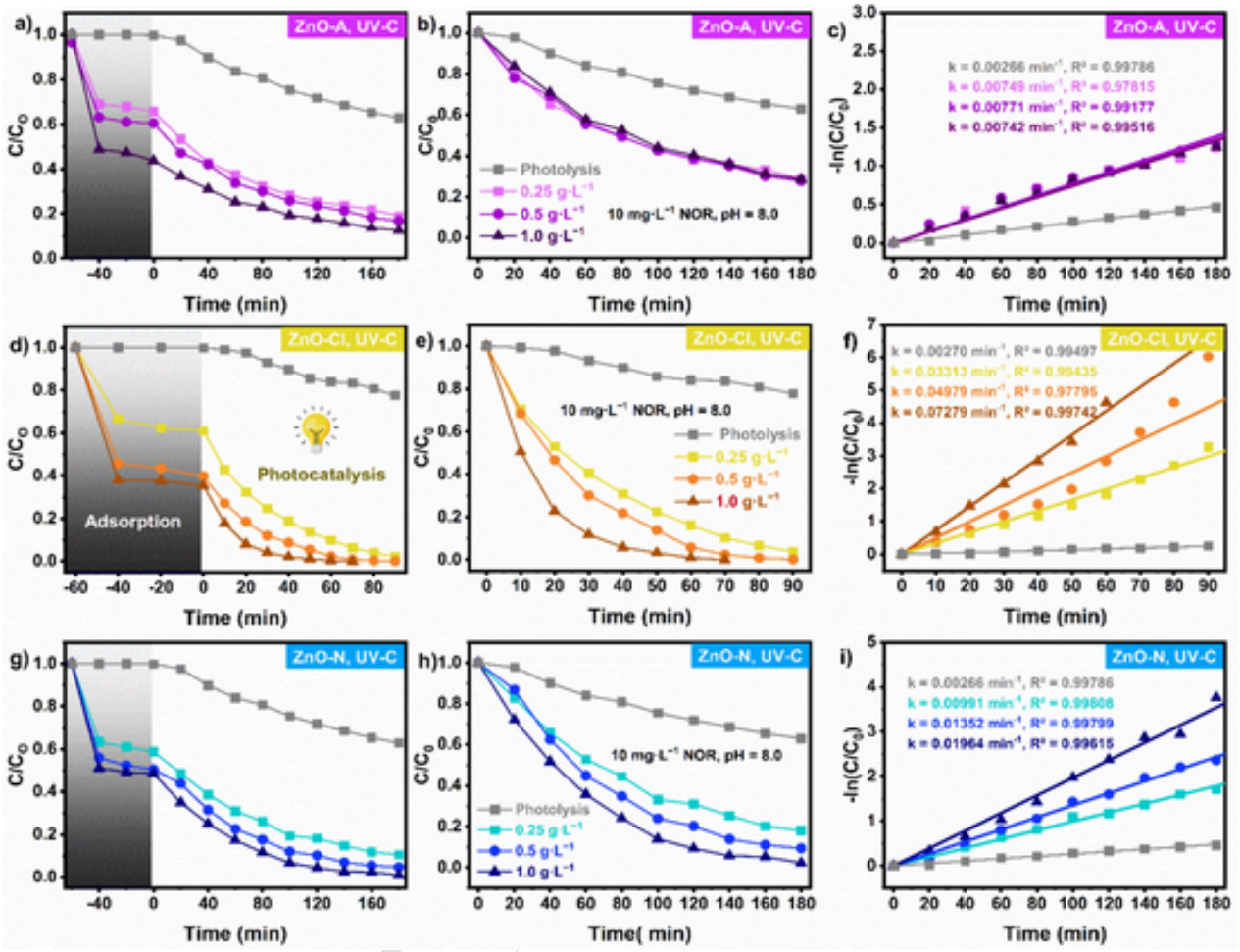

Fig.6. Effect of dosage of catalyst on NOR degradation efficiency (C_o = 10 mg·L^{-1} and pH = 8) for different ZnO photocatalysts: a) ZnO-A, b) ZnO-Cl, and c) ZnO-N at pH = 8.

todegradation tests of NOR were conducted at varying pH from 6 to 10 for ZnO compounds. The photocatalyst dosage and NOR concentration were kept at 0.25 g·L^{-1} and 5 mg·L^{-1}, respectively.

Adsorption and photocatalysis processes of NOR were enhanced in a slightly alkaline environment for the synthesized ZnO compounds (Fig. 8a, d, and g). Regarding the ZnO-A photocatalytic performance, its degradation efficiencies reached 71.7, 76.0, and 73.1 % in 180 min for pH values controlled at 6, 8, and 10, respectively (Fig. 8b). Furthermore, the photodegradation of NOR can be well described by the pseudo-first-order reaction kinetics, $R^2 > 0.97$. The values of k for ZnO-A increased from 0.00808 to 0.01025 min^{-1} as the pH changed from 6 to 8 (Fig. 8c). When ZnO-A photocatalyst was used, the maximum pollutant degradation efficiency was achieved at pH = 8, and the k values decreased slightly with increasing pH to more alkaline conditions, i.e., pH = 10. As was also observed for ZnO-A, ZnO-Cl showed increasing degradation efficiency with an increase in pH from 6 to 8 and then a decrease at pH 10. As shown in Fig. 8e, the ZnO-Cl photocatalytic performance reached 95.5, 100, and 97.2 % in 70 min in the investigated pH range. Under slightly alkaline conditions, ZnO-Cl showed the highest kinetic constant value among the studied photocatalysts, with k = 0.07350 min^{-1} (Fig. 8f). Finally, its degradation was evaluated at different pH levels with the use of ZnO-N as a photocatalyst. After 180-minute UV-C light exposure, the photocatalytic efficiencies of ZnO-N were 91.5, 94.9, and 95.3 % for suspensions containing NOR at pH 6, 8, and 10, respectively (Fig. 8h). Regarding the degradation kinetics of the contaminant, the k values for ZnO-N were between those for ZnO-A and ZnO-Cl, indicating intermediate photocatalytic activity (Fig. 8i).

The processes of adsorption and photocatalysis are influenced by the electrostatic interaction between the pollutant and the surface charge of the photocatalyst [30]. Norfloxacin exists in different pH-dependent ionic forms and has two ionization constants, with pKa values of 6.24 and 8.75 [23,68]. In an aqueous medium, it is in its cationic state when pH < 6.24, corresponding to the protonation of the piperazine ring's amine group, and exists in the zwitterionic form at pH values between pKa_1 and pKa_2 [73]. In its zwitterionic form, its molecule is electrically neutral since it has an equal distribution of charge between protonated (NH_2^+) and deprotonated (COO^-) groups. On the other hand, at pH > 8.75, it exists in anionic form as a result of the deprotonation of the carboxylic group [64]. The point of zero charge (pH_{zpc}) of ZnO is 9.0 ± 0.3 [23]; therefore, ZnO photocatalysts exhibit a negative charge above pH_{zpc} while displaying a positive charge for values below this point [74]. The maximum adsorption for all synthesized samples was observed at pH = 8, corresponding to the zwitterionic form of NOR. At pH = 10.0, the decrease in adsorption is attributed to electrostatic repulsion between the surface charges of ZnO and deprotonated NOR molecules.

In general, our results indicate NOR degradation efficiencies were higher under alkaline conditions than under acidic ones, as also reported by Zhang et al. (2019) [75]. Under acidic conditions, active sites on the catalyst's surface exhibit a low capacity to generate hydroxyl radicals [76]. Acidic medium has a higher concentration of H^+ ions,

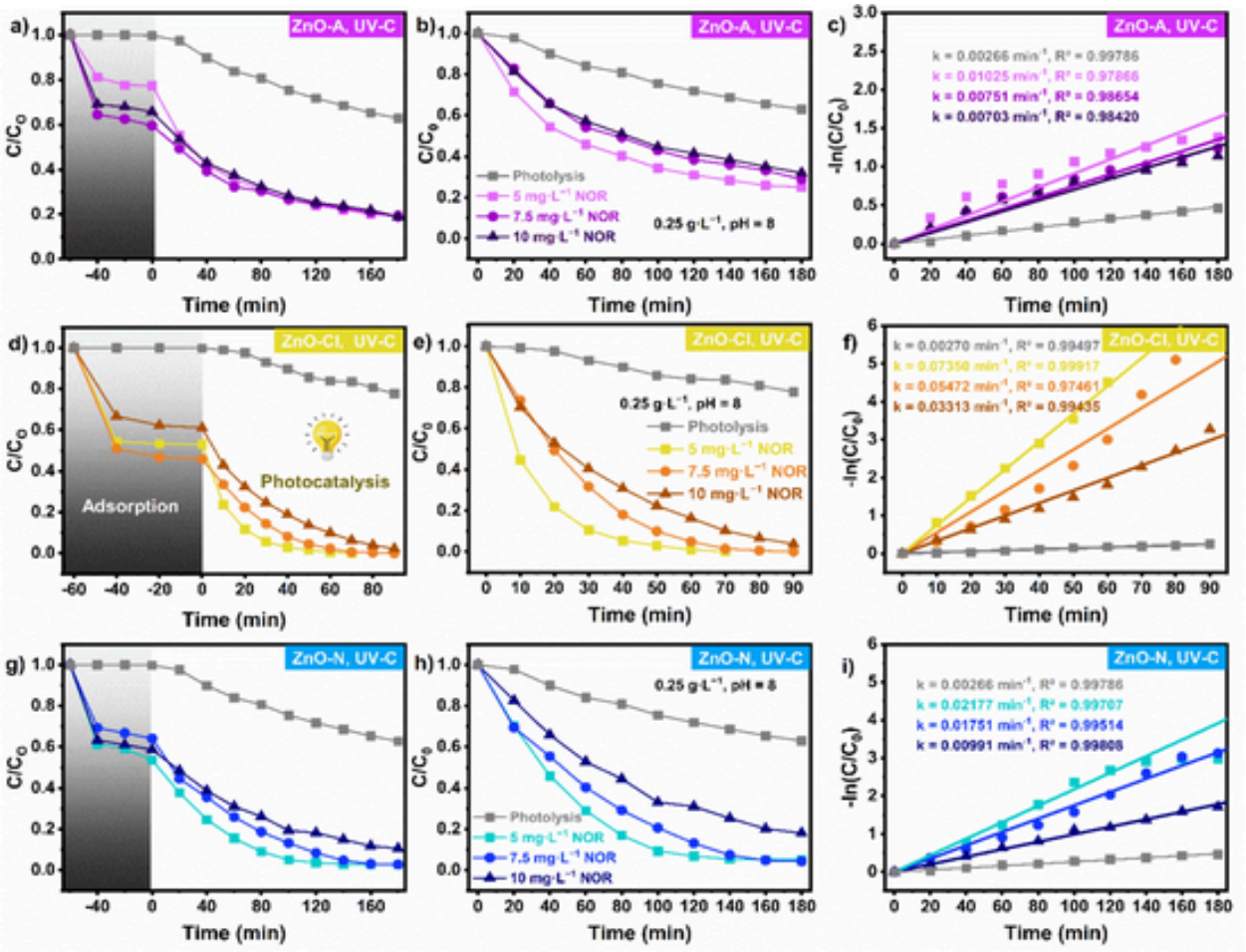

Fig.7. Effect of initial NOR concentration on degradation efficiency (0.25 g·L^{-1} catalyst dosage and pH = 8) for different ZnO photocatalysts: a) ZnO-A, b) ZnO-Cl, and c) ZnO-N at pH = 8.

which have an affinity with hydroxyl anions [27], thus reducing the generation of oxidative species •OH and the efficiency of pollutant degradation [27]. At pH = 6, the electrostatic repulsion between ZnO and the positive charges of NOR hinders its adsorption, leading to lower subsequent degradation efficiency. Enhanced photodegradation under alkaline conditions, on the other hand, occurs due to the reaction of hydroxyl ions with the photo-generated hole, producing more hydroxyl radicals [10]. In terms of reaction, it can be described as:

$$ZnO\,(h+) + OH- \rightarrow \bullet OH + ZnO \quad \text{(R1)}$$

Additionally, the maximum photodegradation efficiency was observed at pH 8 due to the minimization of electrostatic repulsion between the NOR molecule and the photocatalyst surfaces. At such a pH, NOR assumes the zwitterionic form and has a lower barrier for adsorption. Under conditions of pH > pH_{zpc}, as seen for pH = 10, the degradation efficiency of ZnO photocatalysts decreases due to electrostatic repulsion between the negative charges of the NOR molecule and those on the photocatalyst surfaces [64]. An excess of OH^- can compete with NOR for active sites on the catalyst's surface under highly alkaline conditions, thereby reducing the photocatalytic rate [77]. The pH of effluents containing trace amounts of antibiotics in wastewater often ranges between neutral and slightly alkaline, following industrial and hospital effluent disposal guidelines [78]. Moreover, a pH around 8 is the natural condition of the NOR solution. In function of those considerations and the high efficiency of ZnO photocatalysts for NOR degradation at pH = 8, this pH value was selected as the optimal one for the photocatalysis experiments performed.

3.3. Mechanism of norfloxacin photocatalytic degradation

Different scavenger agents were employed towards the understanding of the photodegradation mechanism of NOR and the identification of the reactive species involved (Fig. 9a). ZnO-Cl pH = 8, which showed the highest removal and the highest *k* value in NOR photodegradation assays, was chosen as a reference. The highest NOR degradation (100 %) occurred in the absence of any scavenger and decreased to 97.5 % when $AgNO_3$ was used as a scavenger, thus suggesting a minor role of electrons (e^-). The small influence of electrons on scavenger experiments indicates a low rate of recombination of the electron-hole pair and that photogenerated electrons in the conduction band react with dissolved oxygen to form superoxide radicals before recombining with the h^+ present in the valence band – $O_2\bullet^-$ is one of the active species in the mechanism. The minimization of the recombination of photogenerated e^-/h^+ pairs is evidenced by high efficiency and higher kinetic constants [79]. Conversely, a more pronounced efficiency drop was observed when h^+, $\bullet O_2^-$, and •OH scavenger agents were added, indicating they are active species produced and responsible for NOR degradation. The sequence of contribution of each reactive species to NOR degradation was •OH > $\bullet O_2^-$ > h^+ > e^-, highlighting the importance of •OH radicals in the photocatalysis process.

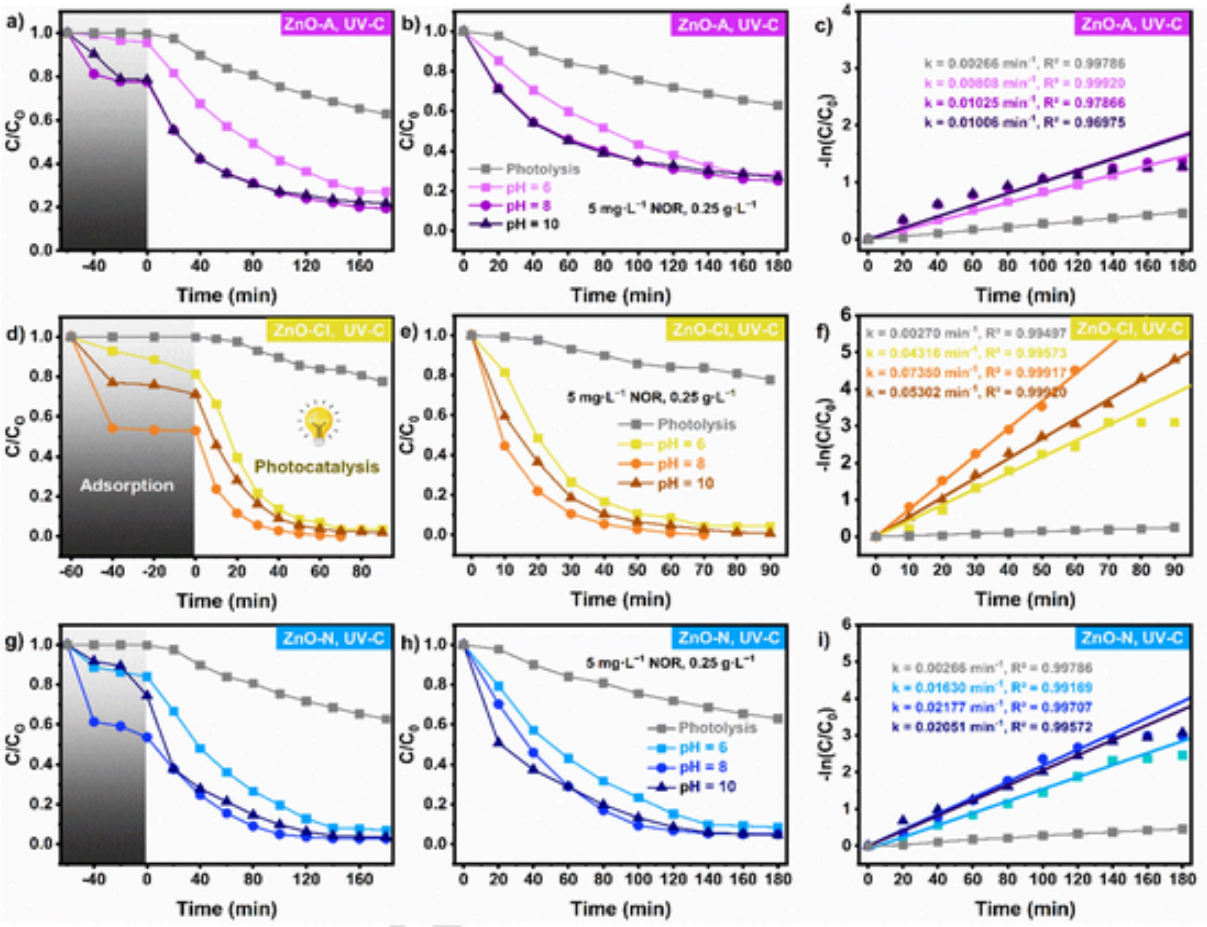

Fig.8. Effect of pH on NOR degradation efficiency (0.25 $g{\cdot}L^{-1}$ catalyst dosage and initial NOR concentration of 5 $mg{\cdot}L^{-1}$).

To identify potential free radicals generated in the photocatalysis system, EPR experiments were conducted using DMPO as a spin trap, as depicted in Fig. 9b. Under dark conditions, no significant EPR signals were detected, indicating the absence of radical species formation. Then, three distinct conditions were investigated: 1) photolysis of an aqueous solution of norfloxacin (NOR + DMPO); 2) irradiation of an aqueous ZnO dispersion (ZnO + DMPO); and 3) a photocatalytic experiment using ZnO nanogranules as a UV-C irradiated photocatalyst for NOR degradation (NOR + ZnO + DMPO). In all these conditions, adducts of DMPO-OH and DMPO-$(OH)_2$ have been identified, but in varying quantities, providing insights into the generation mechanisms and production efficiency of these reactive species.

DMPO-OH adducts were identified as a four-line (1:2:2:1) pattern with hyperfine coupling constants (a_N = 15.2 ± 0.2 G and a_H = 14.8 ± 0.2 G). On the other hand, the 1:1:1 triplet signal suggests the presence of three equivalent hydrogens of the CH_3 group and two OH groups to unpaired electrons on the NO fragment, characteristic of the DMPO-$(OH)_2$ adduct [80]. The coupling constants for the DMPO-$(OH)_2$ adduct are a_N = 15.1 ± 0.2 G, a_H = 0.80 ± 0.05 G (H of OH), and a_H = 0.61 ± 0.05 G (H of CH_3). The triplet signal corresponding to the DMPO-$(OH)_2$ adduct may be the result of two consecutive addition reactions involving •OH radicals [80] and/or the dimerization of the DMPO molecule [81].

A higher relative intensity of the EPR signals for reactive radicals indicates a higher yield of these species [82]. In the NOR photolysis experiment, a lower amount of DMPO-OH and DMPO-$(OH)_2$ adducts was observed. This can be attributed to the limited production of •OH radicals by the direct decomposition of NOR under UV-C irradiation. In contrast, the irradiation of ZnO nanogranules under UV-C light resulted in a higher concentration of DMPO-OH and DMPO-$(OH)_2$ adducts, indicating that the •OH radicals can be generated on the surface of the ZnO nanogranules by the reaction of the photogenerated holes in the valence band and hydroxyl groups with water. It is interesting to note that in the presence of NOR, the amount of •OH radicals captured by DMPO decreased compared to the photocatalytic experiment conducted in the absence of the target contaminant. This suggests that there is a competitive reaction between NOR and DMPO for the •OH radicals. Similar results have been observed in previous studies for other FQs compounds [83].

Under photocatalytic reaction, the reduction in the intensity of the DMPO-OH adduct suggests that NOR degradation occurs mainly due to the direct attack of NOR molecules by the •OH radicals generated on the photocatalyst surface before these radicals are captured by DMPO. The •OH radical is known for its electrophilic nature and has a strong affinity for electron-rich sites of molecules, in particular for aromatic molecules[84], as NOR.These findings provide valuable insights into the mechanisms involved in the photocatalytic degradation of norfloxacin and the interactions of free radicals with the reaction medium.

In EPR analysis, DMPO is a non-selective spin trap widely used to detect free radicals, such as, the hydroxyl radical and superoxide. The hydroxyl radical, in particular, tends to react more quickly with DMPO than the superoxide radical. This may result in a predominance in the concentration of DMPO-OH adducts in the EPR spectrum, making it difficult to identify the DMPA-OOH from the superoxide radical. Furthermore, DMPO-OOH adducts, formed from the reaction between DMPO and superperoxide radicals, are less stable and can decompose quickly

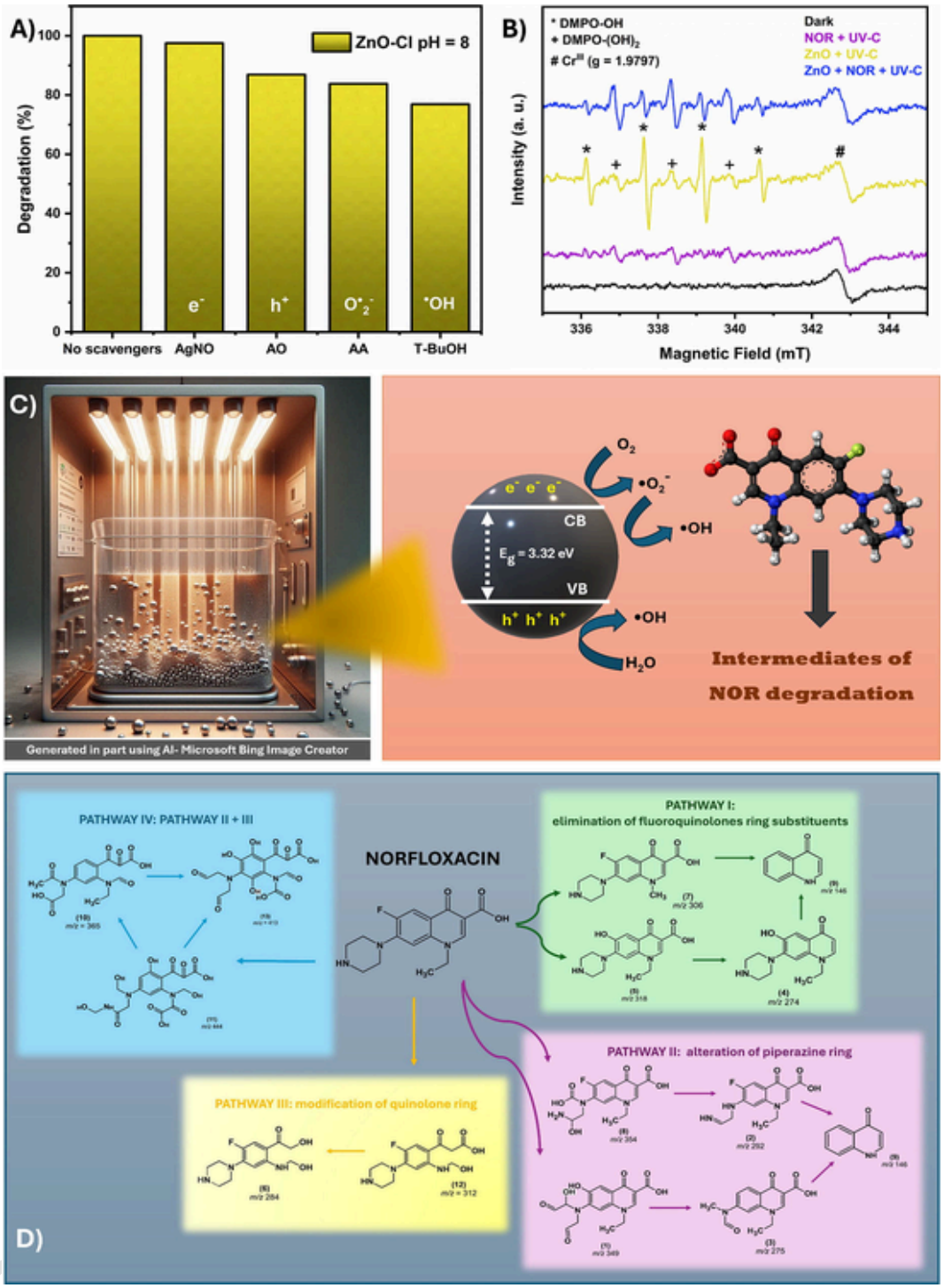

Fig.9. (a) NOR degradation efficiency in the presence of different scavengers (e^-, h^+, $\bullet O_2^-$, and $\bullet OH$); (b) Identification of radicals by EPR; (c) Proposed mechanism of ROS photocatalytic production for NOR degradation; (d) Degradation pathways of NOR using ZnO nanogranules as a photocatalyst.

or undergo other secondary reactions that do not allow their detection in such an effective manner in the aforementioned technique [85]. The DMPO-superoxide adduct is unstable and spontaneously decomposes, yielding a non-radical species and DMPO-OH [86]. Radicals, such as, $HO_2\bullet$ and $\bullet O_2^-$ are highly unstable in water and tend to undergo disproportionation rapidly rather than reacting slowly with DMPO [87]. Although superperoxide radicals have not been detected by the EPR technique, their formation cannot be ruled out since they were identified when ascorbic acid was used in scavenger experiments. The results of EPR as well as the scavengers suggest the determining role of hydroxyl radicals in the photocatalytic degradation of NOR when ZnO nanogranules were used as a photocatalyst.

To describe the possible photocatalytic degradation mechanism of norfloxacin under UV-C light, the energy levels of the conduction band (E_{CB}) and valence band (E_{VB}) of ZnO nanogranules were determined using the following equations:

$$E_{VB} = \chi - E_e + 0.5E_g \quad (2)$$
$$E_{CB} = E_{VB} - E_g \quad (3)$$

where E_g is the semiconductor band gap, E_{VB} and E_{CB} are the VB and CB edge potentials, respectively. E_e is a constant relative energy of free electrons on the standard hydrogen electrode potential (E_e = 4.5 eV), and χ, also known as Mulliken electronegativity, is the geometric mean of the absolute electronegativity of each atom within the semiconductor. Since χ_{Zn} = 4.5 eV and χ_O = 7.54 eV, so χ_{ZnO} = 5.79 eV [88]. The energy gap (E_g) value for ZnO nanogranules was determined to be 3.32 eV from the Tauc plot (Fig. 4b). Therefore, the E_{VB} and E_{CB} values for the nanogranules were calculated as + 2.95 eV and −0.37 eV, respectively, relative to the normal hydrogen electrode (NHE).

Fig. 9c illustrates the photocatalytic process using ZnO nanogranules. When exposed to UV-C light with energy higher than the band gap, electronic transfer occurs, promoting an electron from the VB to the CB and generating an electron-hole pair. These charge carriers – electrons (e^-) in the CB and holes (h^+) in the VB – migrate to the surface of the ZnO photocatalyst, where redox reactions take place. As the energy level of the VB (E_{VB} = 2,95 eV) of ZnO nanogranules is more positive than the standard redox potential of $H_2O/•OH$ (E_0 = +2.33 eV *vs.* NHE), •OH radicals are formed by the reaction of h^+ with water molecules in the VB. Simultaneously, the CB energy level is more negative than the standard redox potential of $O_2/•O_2^-$ (E_0 = -0.33 eV *vs.* NHE). Consequently, excess electrons on the ZnO surface can interact with dissolved oxygen molecules, forming the $•O_2^-$ radical due to its lower conduction band edge potential (−0.37 eV *vs.* NHE) compared to the standard potential E_0 ($•O_2^-/O_2$) (−0.33 eV *vs.* NHE). The EPR spectra of ZnO nanogranules confirm significant signals of the •OH radical. Two plausible explanations exist for this observation: firstly, photogenerated holes may capture OH^- ions to produce •OH radicals [89]. Secondly, the resulting $•O_2^-$ radical undergoes protonation, leading to the formation of hydroperoxyl radicals ($HO_2•$), and subsequently, H_2O_2, which dissociates into highly reactive •OH species [27]. The main reactions involved in NOR degradation can be summarized as follows:

$$ZnO + h\upsilon \rightarrow ZnO\ (e^-_{CB} + h^+_{VB}) \quad (R2)$$
$$h^+ + OH^- \rightarrow {}^{\bullet}OH \quad (R3)$$
$$h^+ + H_2O \rightarrow •OH + H^+ \quad (R4)$$
$$e^- + O_2 \rightarrow •O_2^- \quad (R5)$$
$$NOR + h^+ + •OH + •O_2^- \rightarrow \text{Intermediates of NOR degradation} \quad (R6)$$

3.4. Investigation of NOR degradation pathways

As shown in Table 1, the LC-MS results indicate degradation with ZnO-Cl at pH 8, resulting in the generation of thirteen primary compounds (Figs. S1–S13). Seven of those intermediates (**2, 4–9**) have already been reported in other studies on the photocatalytic degradation of NOR [90,91,92], whereas intermediates **1, 3, 10–13** are being reported for the first time.

According to the structures of the intermediates identified, the degradation of NOR via ZnO-Cl pH = 8 proceeded through four distinct pathways (Fig. 9d), namely, I) elimination of fluoroquinolone ring substituents, II) modification of the quinolone ring, and III) alteration of the piperazine ring. The latter two routes occurred separately and in conjunction, leading to pathway IV and yielding compounds **10**, **11**, and **13**.

In pathway I, the oxidizing species (•OH and $•O_2^-$) generated on the photocatalyst surface attack several carbon bonds within the fluoroquinolone ring, leading to the formation of the following intermediate compounds: compound **5** (*m/z* 318), generated through a fluorine elimination process; compound **4** (*m/z* 274), produced via simultaneous defluorination and decarboxylation reactions; and compound **7** (*m/z* 306), formed from the release of a methyl group (–CH_3) [90,91].

Table 1
LC-MS/MS data for the intermediate compounds detected during photocatalysis of norfloxacin by ZnO-Cl pH = 8.

Intermediate	Rt (min)	Molecular Ion $[M+H]^+$	Main Fragments (*m/z*)
1	0.50	349	306, 275, 232, 191, 102, 83, 59
2	1.01	292	275, 100, 83, 59
3	2.48	275	100, 83, 59
4	6.30	274	100, 83, 59
5	6.40	318	100, 83, 59
6	7.35	284	100, 83, 59
7	7.85	306	100, 83, 59
8	7.96	354	115, 100, 83, 59
9	8.11	146	105, 83, 59
10	8.37	365	105, 83, 59
11	8.42	444	400, 146, 105, 83, 59
12	8.79	312	146, 105, 74, 59
13	8.94	413	146, 105, 74, 59

In pathway II, the attack of oxidizing radicals resulted in the cleavage of the C-N bond of the piperazine ring, followed by addition and elimination reactions within the ring. The formation of intermediate **8** with *m/z* 354 is proposed to occur through oxidation and hydroxylation of the piperazine ring [92]. The subsequent release of OH and acidic groups from **8** generated compound **2** with *m/z* 292. Pathway II also occurred in conjunction with defluorination, as evidenced by compounds **1** (*m/z* 349) and **3** (*m/z* 275). The proposed formation of **1** involves hydroxylation of the NOR molecule, followed by fluorine elimination, oxidation, and removal of the ammonia moiety from the piperazine ring. Decarboxylation and subsequent release of the hydroxyl unit, as water, from compound 1 gave rise to 3.

The lower molecular intermediate quinolinone (**9**) is a derivative of pathways I and II [90]. Its proposed formation with a molecular ion of *m/z* 146 involves the elimination of fluorine from compounds 2 and 7 or hydroxyl from 4, along with de-carboxylation, de-piperazinylation, and de-methylation or de-ethylation from the quinolone ring from compounds 2, 3, 4, or 7.

During the degradation of NOR with the use of ZnO-Cl pH = 8, an initial hydroxylation reaction was observed in the fluoroquinolone ring of the molecule, leading to the rupture of the structure (Pathway III). Under such conditions and with the loss of a methyl group, compounds with *m/z* 312 (**12**) and *m/z* 284 (**6**) were detected.

Pathway IV was detected in intermediates **10** (*m/z* 365), **11** (*m/z* 444), and **13** (*m/z* 413). Their formation involves the attack of OH on the C = C double bond adjacent to the carboxylic acid group on the quinolone ring, cleavage of the C-N bond with the opening of the piperazine ring, and successive oxidation and hydroxylation reactions on the rings with the elimination of functional groups. The cleavage of C = C with subsequent oxidation of the carbons involved in this bond is among the mechanisms reported in the literature for the generation of NOR intermediates [91,93,94]. Additionally, the opening of the piperazine ring, accompanied by oxidation and/or hydroxylation of the carbons bonded to the nitrogens, as well as oxidation and/or hydroxylation of the methyl group linked to the quinolone ring, has been reported in other studies on NOR degradation [91,93,94,95].

3.5. Investigation into the superior photocatalytic performance exhibited by ZnO nanogranules compared to other synthesized morphologies

EIS, employing Nyquist impedance plots and Bode-phase analysis, was used to investigate the interfacial properties and charge recombination behavior of synthesized ZnO NPs. The analysis of the Nyquist data (Fig. 10a) and the simulated circuit (Fig. 10b) suggests that ZnO-Cl (85.6 KΩ) has the lowest electron transfer resistance compared to ZnO-

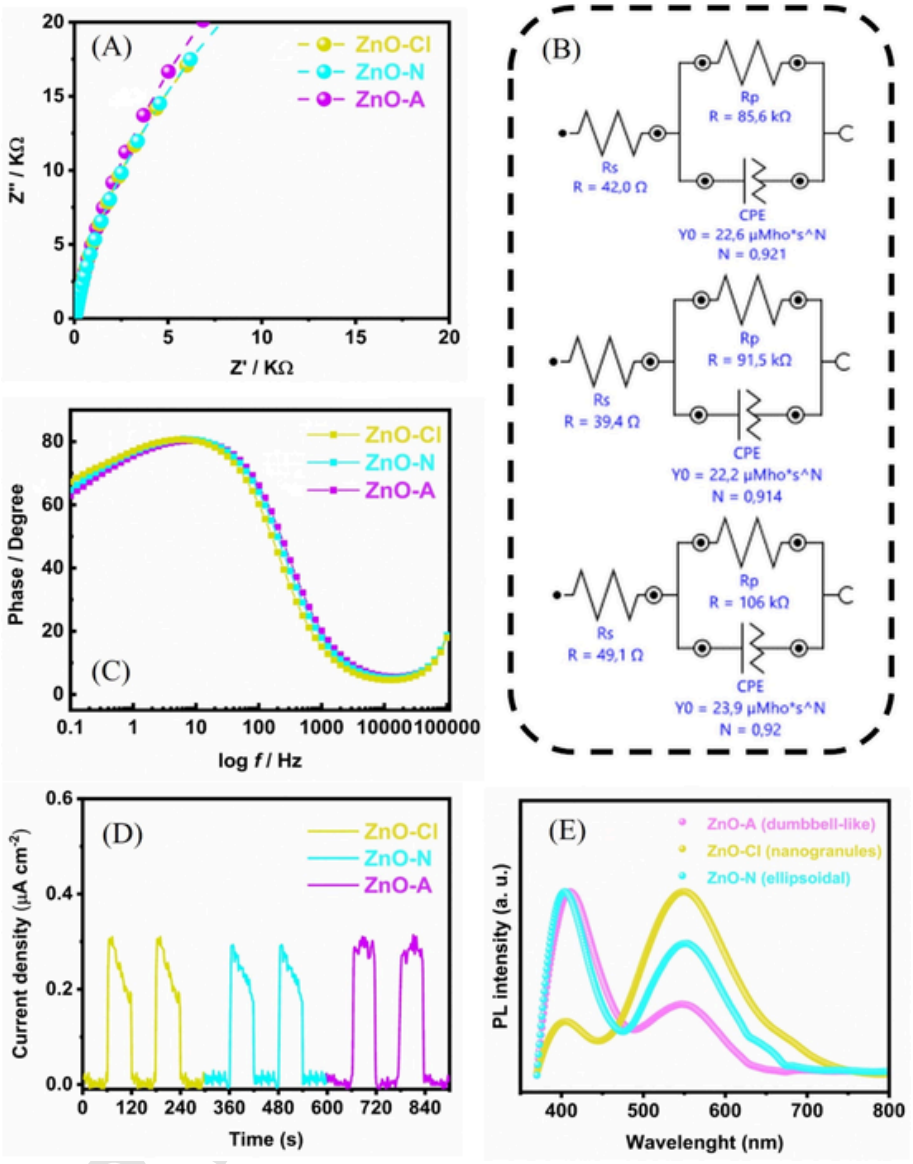

Fig.10. (a) EIS curves, (b) equivalent circuits used to simulate the EIS experimental data (c) Bode-phase plots, (d) chronoamperometry curves, and (e) PL spectra of ZnO samples.

A (106.0 KΩ) and ZnO-N (91.5 KΩ) NPs. This translates to faster degradation kinetics of the NOR drug by the photocatalytic activity of these NPs, potentially explaining the findings of this work [96].

Following these observations, the Bode-phase plots for the synthesized ZnO NPs (Fig. 10c) were analyzed. Interestingly, a shift in the maximum phase angle frequency (f) was observed between the ZnO-A, ZnO-Cl, and ZnO-N samples, which exhibited peak frequencies of 10.0, 6.31, and 7.94 Hz, respectively. Considering this analysis, the lifetime of the photogenerated electrons (t_e) for these NPs was then calculated using Equation (2) [97].

$$t_e = 1/(2\,\pi\, f) \quad (4)$$

The calculated t_e for ZnO-A, ZnO-Cl, and ZnO-N were 0.016, 0.025, and 0.020 s, respectively, and these results indicate that ZnO-Cl (nanogranules) possesses the longest charge carrier lifetime. A longer lifetime signifies a beneficial separation of charges, leading to a reduced recombination rate and increasing their photocatalytic activity [98]. Long-lived photogenerated carriers can quickly reach active sites on the surface to participate in photocatalytic reactions [89].

To further investigate the photocatalyst profile for these ZnO NPs, photocurrent measurements were performed using chronoamperometry, as shown in Fig. 10d. Upon illumination with an 8 W UV-C lamp, all three synthesized ZnO NPs exhibited an initial current response of approximately 0.3 $\mu A{\cdot}cm^{-2}$. However, ZnO-Cl displayed a current decay of 0.13 $\mu A{\cdot}cm^{-2}$ during irradiation, while ZnO-N lost 0.09 $\mu A{\cdot}cm^{-2}$, and the ZnO-A NPs maintained a stable current. The observed current decay corresponds to the ease of electron generation and release in the medium. This finding aligns with degradation tests, indicating that ZnO-Cl NPs exhibit superior photocatalytic activity attributed to their efficient charge separation [99].

Photoluminescence spectroscopy (PL) is a valuable technique for evaluating the separation efficiency of the photogenerated charge carriers in semiconductors as well as identifying the formation of defects [100,101]. Fig. 10e shows the PL spectra of ZnO nanostructures synthesized from different zinc precursors. The measurements were carried out with an excitation of 325 nm, which corresponds to an energy of 3.81 eV, higher than the energy band gap of ZnO (E_g = 3.19 – 3.32 eV). This allows electrons in the ZnO valence band to easily transit

into the conduction band when excited, creating electron-hole pairs [102]. PL spectra reveal emissions in three distinct regions: one in the UV and two in the visible. The emission in the UV region is attributed to the transition near the edge of the ZnO energy band [103], while the visible emissions are associated with nanostructured ZnO surface defect states [104]. The emission in the UV region is due to radiative recombination of electrons and holes in the conduction band and valence, respectively, known as near-end emission of the band (NBE), which was observed around 400 nm [105,106,107]. A weak intensity of PL attributed to the NBE band is generally assigned to a lower electron-hole recombination rate under light irradiation [108]. Among the obtained morphologies, ZnO nanogranules exhibit a lower radiative recombination of photogenerated electrons and holes. This reduced rate of hole-electron pair recombination in ZnO nanogranules can be attributed to their smaller particle size. Small particles offer shorter paths for charge carriers to reach the surface where photocatalytic activity occurs [109]. This reduction in carrier migration distance decreases the likelihood of recombination of active charges (electron-hole pairs), thereby enhancing the photocatalytic efficiency [109]. The broad green emission band observed at 550 nm in ZnO nanostructures is attributed to the presence of defects, particularly ionized oxygen vacancies [106]. The intensity of this green emission is notably higher in ZnO nanogranules (ZnO-Cl) compared to other morphologies, indicating a greater concentration of oxygen vacancies [106]. Oxygen vacancies are known to act as traps that capture photo-excited electrons, thereby reducing recombination with holes [109,110]. Surface oxygen vacancies also serve as charge traps and adsorption sites, facilitating the transfer of charges to adsorbed compounds [111]. This mechanism effectively suppresses the recombination of photogenerated charge carriers, leading to enhanced photocatalytic performance [111]. In addition, the red emission around 650 nm observed for ZnO nanostructures is attributed to the presence of oxygen interstitials, indicating the existence of additional structural defects [104]. The highest concentration of defects on the surface of ZnO nanogranules can be attributed to the smaller particle size and larger surface area, consistent with the results of SEM/MET and BET, respectively.

3.6. Reusability and stability of ZnO nanogranules as a photocatalyst

In practical applications, the reusability of photocatalysts is a crucial aspect to be considered. As shown in Fig. 11a, the degradation efficiency of the most efficient photocatalyst, i.e., ZnO-Cl pH = 8 (nanogranules), remained virtually unchanged even after three cycles. No insignificant reduction in photocatalytic activity was observed, since it decreased only 3 % from the first to the third cycle, suggesting a notable cycling stability of the studied photocatalyst. Additionally, the stability of ZnO nanogranules was assessed by comparing the degradation rate constants over three consecutive reaction cycles. It was found that there was no significant decay in the kinetic constants from one cycle to another, with values of k_1, k_2, and k_3 were 0.07350 (R^2 = 0.99917), 0.07244 (R^2 = 0.99201), and 0.07076 (R^2 = 0.99525), respectively. After three cycles of recycling, the crystal structure of ZnO nanogranules was examined using XRD to assess their stability. No significant changes in peak shape were observed, and all peaks were indexed according to the crystallographic data (JCPDS No. 36–1451), indicating the structural stability of the hexagonal

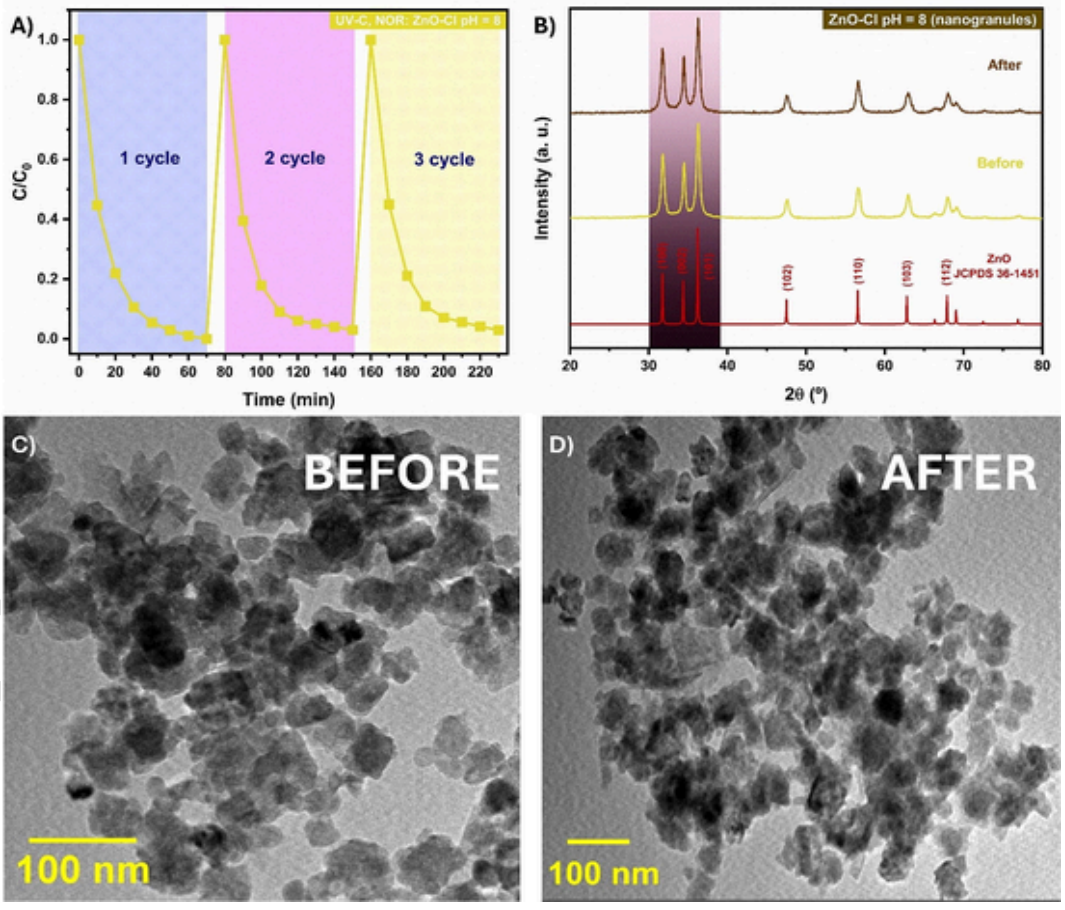

Fig.11. (a) Recycle efficiency, (b) XRD patterns, and (c, d) TEM images after the use of ZnO nanogranules as a photocatalyst under multiple cycles of NOR degradation.

Table 2
Comparative studies of NOR photocatalytic degradation using different photocatalysts under UV-light irradiation.

Photocatalyst	Morphology	Illumination source	NOR initial concentration ($mg{\cdot}L^{-1}$)	Photocatalyst dosage ($g{\cdot}L^{-1}$)	Photocatalysis pH	Degradation efficiency (%)	Time of degradation (min)	$k \cdot 10^{-2}$ (min^{-1})	Ref.
ZnO/ZnS@BC	irregular circles and tetragonal crystals	UV lamps, n/a	25	0.5	7	55	180	2.12	[28]
CuO/ZnO/ g-C_3N_4	spherical	UV-A (3 W, 395 nm)	7.5	2.0	7	93.7	120	n/a	[65]
Ni doped ZnO	Nanoparticle	UV-A (9 W, 390 nm)	5	n/a	n/a	98	120	n/a	[113]
Fe_3O_4/C/ZnO	Nanoparticle	UV-A (20 W, 365 nm)	10	1.0	n/a	97	60	n/a	[114]
ZnO/ZnS	spherical	UV (125 W, n/a)	10	0.25	n/a	45	240	0.02	[29]
TiO_2 P25	n/a	UV-A (250 W, 365 nm)	150	n/a	7	45	210	n/a	[115]
TiO_2/Ti film	sheet-like	UV-C (10 W, 254 nm)	10	n/a	n/a	98.9	90	5.04	[116]
ZnS-rGO	3D ZnS nanospheres decorated with rGO nanosheet	UV (300 W, n/a)	20	1.0	n/a	92	240	n/a	[117]
Ni_5P_4 coupled g-C_3N_4 quantum dots (GCNQDs)	porous flower spherical	UV (1000 W, n/a)	30	0.6	7	92	120	2.18	[69]
Mn:ZnS QDs	nanoparticle	UV (40 W, UV-C)	15	2.4	10	86	60	3.21	[64]
BiOCl	spherical	UV (125 W, n/a)	10	0.25	n/a	92	240	1.80	[118]
SDS capped BiOCl	spherical	UV (125 W, n/a)	10	0.25	7.54	94	240	1.14	[16]
BiOCl	nanosheets	UV (300 W, n/a)	10	1.0	n/a	84	180	1.0	[119]
CTAB capped BiOCl	microsphere	UV (125 W, n/a)	10	0.25	7.54	98	240	4.81	[16]
ZnO	nanogranules	UV-C (15 W, 254 nm)	5	0.25	8	100	70	7.35	This work

wurtzite phase (Fig. 11b). Furthermore, morphological evaluation via TEM was conducted after the third cycle, revealing no significant changes in relation to the initial microstructure (Fig. 11c–d). Thus, the ZnO nanogranule-based photocatalysts synthesized in this study exhibit outstanding stability and efficiency after multiple cycles of photocatalytic NOR degradation.

3.7. Comparative photocatalytic performance of ZnO nanogranules with other photocatalytic materials for NOR degradation under UV-light

ZnO nanogranules exhibit exceptional performance and offer several advantages over other photocatalysts, as shown in Table 2. Most studies in Table 2 investigate degradation at concentrations much higher than those typically found in the environment. For example, this pollutant has been detected in different water matrices of India, with concentrations of 420 $\mu g{\cdot}L^{-1}$ in treated wastewater, 520 $\mu g{\cdot}L^{-1}$ in surface water, and 0.145 $\mu g{\cdot}L^{-1}$ in groundwater [112]. In new photocatalysis experiments using ZnO nanogranules at 20 ppm and 30 ppm of NOR, degradation reached 88.2 % and 66.6 % in 70 min (Fig. S14), respectively, outperforming the listed materials. Although these concentrations are higher than environmental levels, our results demonstrate that nanogranules perform well across a wide range of contaminant concentrations. They achieved a remarkable 100 % degradation efficiency within 70 min when 5 $mg{\cdot}L^{-1}$ of NOR was used, surpassing all other photocatalysts.

These nanogranules exhibit impressive reusability, maintaining structural and morphological stability after multiple recycling tests, as detailed in § 3.6. Their stability ensures prolonged efficacy, making them a reliable choice for continuous environmental remediation applications. They are cost-effective and involve a simpler composition since they do not require complex combinations with other materials, such as forming heterostructures or doping strategies. The formation of composite materials and heterostructures has been a commonly employed strategy to enhance photocatalytic performance. However, achieving practical applications with these photocatalysts often requires long degradation times and/or high-powered lamps, as shown in Table 2. Moreover, their simplicity in synthesis and single-material composition not only reduces costs but also enhances reproducibility and scalability for large-scale implementation in wastewater treatment systems. Therefore, their outstanding performance, coupled with their cost-effectiveness and simple synthesis, underscores their potential as highly efficient and practical photocatalysts for NOR degradation and other environmental remediation applications.

4. Conclusions

This investigation employed a straightforward hydrothermal method to induce morphological variations in pure ZnO nanostructures, guided by the alteration of zinc precursor salts. Such morphological changes, influenced by counterions, significantly impacted the surface area. Notably, the limited documentation on the use of pure ZnO nanostructures for an effective and swift degradation of NOR under UV-C light underscores the novelty of this study. According to the findings, pure ZnO nanoparticles demonstrated photocatalytic activity comparable to or surpassing that of ZnO nanocomposites, heterojunctions, and doped ZnO in Norfloxacin degradation under UV-light conditions. Factors such as photocatalyst dosage, initial contaminant concentration, and pH in photocatalysis experiments were meticulously investigated. Optimal dosages for ZnO-A, ZnO-Cl, and ZnO-N were determined by considering both efficient degradation and cost-effectiveness. The initial NOR concentration significantly impacted degradation efficiency, with a 5 $mg{\cdot}L^{-1}$ optimal concentration. Additionally, the solution pH played a crucial role, with alkaline conditions (pH = 8) proving most favorable for enhanced degradation due to minimized electrostatic re-

pulsion between the surface charges of ZnO and NOR molecules. ZnO synthesized from the chloride precursor showed the highest degradation rate of Norfloxacin under UV-C light, e.g., 100 % in 70 min. Based on BET, EIS, and PL measurements, the superior photocatalytic performance exhibited by ZnO nanogranules can be attributed to the synergistic effects of reduced electron-hole pair recombination, increased surface area, and higher concentration of crystalline defects.

CRediT authorship contribution statement

Ramon Resende Leite: Writing – review & editing, Writing – original draft, Visualization, Methodology, Investigation, Formal analysis, Conceptualization. **Renata Colombo:** Writing – review & editing, Writing – original draft, Visualization, Methodology, Investigation, Formal analysis. **Fausto Eduardo Bimbi Júnior:** Writing – review & editing, Writing – original draft, Visualization, Methodology, Investigation. **Marcos Roberto de Vasconcelos Lanza:** Writing – review & editing, Resources, Funding acquisition. **Hernane da Silva Barud:** Writing – review & editing. **Conrado Ramos Moreira Afonso:** Writing – review & editing, Methodology, Conceptualization. **Maria Inês Basso Bernardi:** Writing – review & editing, Supervision, Resources, Project administration, Funding acquisition.

Declaration of competing interest

The authors declare that they have no known competing financial interests or personal relationships that could have appeared to influence the work reported in this paper.

Data availability

Data will be made available on request.

Acknowledgements

This research was financially supported by São Paulo Research Foundation (FAPESP) [2013/07296-2], National Council for Scientific and Technological Development (CNPq) [303943/2021-1 and 301427/2022-4] and partially financed by the Coordination for the Improvement of Higher Education Personnel (CAPES) , Finance Code 001. The authors are also grateful to Dr. Otaciro Rangel Nascimento for conducting the EPR measurements and for his assistance in discussing these data, and to Dr. Leonnam Gotardo Merizio for the photoluminescence (PL) measurements.

Appendix A. Supplementary data

Supplementary data to this article can be found online at https://doi.org/10.1016/j.cej.2024.154374.

References

[1] UNESCO, The United Nations World Water Development Report 2024: water for prosperity and peace, World Bank, Washington, DC, 2024. https://www.unwater.org/publications/un-world-water-development-report-2024.
[2] P. Greve, T. Kahil, J. Mochizuki, T. Schinko, Y. Satoh, P. Burek, G. Fischer, S. Tramberend, R. Burtscher, S. Langan, Y. Wada, Global assessment of water challenges under uncertainty in water scarcity projections, Nat. Sustain. 1 (2018) 486–494, https://doi.org/10.1038/s41893-018-0134-9.
[3] S. Ahuja (Ed.), Overview: Modern Water Purity and Quality, Handb. Water Purity Qual., Elsevier, in, 2021, pp. 1–18, https://doi.org/10.1016/B978-0-12-821057-4.00014-8.
[4] D. Grey, D. Garrick, D. Blackmore, J. Kelman, M. Muller, C. Sadoff, Water security in one blue planet: twenty-first century policy challenges for science, Philos. Trans. r. Soc. A Math. Phys. Eng. Sci. 371 (2013) 20120406, https://doi.org/10.1098/rsta.2012.0406.
[5] UNICEF, Progress on household drinking water, sanitation and hygiene 2000–2022: special focus on gender, 2023. https://www.unicef.org/wca/media/9161/file/jmp-2023-wash-households-launch-version.pdf.
[6] D.T. Ruziwa, A.E. Oluwalana, M. Mupa, L. Meili, R. Selvasembian, M.M. Nindi, M. Sillanpaa, W. Gwenzi, N. Chaukura, Pharmaceuticals in wastewater and their photocatalytic degradation using nano-enabled photocatalysts, J. Water Process Eng. 54 (2023) 103880, https://doi.org/10.1016/j.jwpe.2023.103880.
[7] A. Gil, L. Galeano, M. Vicente (eds), Applications of Advanced Oxidation Processes (AOPs) in Drinking Water Treatment. the Handbook of Environmental Chemistry vol 67 (2019), https://doi.org/10.1007/978-3-319-76882-3.
[8] L. Rizzo, S. Malato, D. Antakyali, V.G. Beretsou, M.B. Đolić, W. Gernjak, E. Heath, I. Ivancev-Tumbas, P. Karaolia, A.R. Lado Ribeiro, G. Mascolo, C.S. McArdell, H. Schaar, A.M.T. Silva, D. Fatta-Kassinos, Consolidated vs new advanced treatment methods for the removal of contaminants of emerging concern from urban wastewater, Sci. Total Environ. 655 (2019) 986–1008, https://doi.org/10.1016/j.scitotenv.2018.11.265.
[9] V.-A. Thai, V.D. Dang, N.T. Thuy, B. Pandit, T.-K.-Q. Vo, A.P. Khedulkar, Fluoroquinolones: Fate, effects on the environment and selected removal methods, J. Clean. Prod. 418 (2023) 137762, https://doi.org/10.1016/j.jclepro.2023.137762.
[10] L. Tang, J. Wang, G. Zeng, Y. Liu, Y. Deng, Y. Zhou, J. Tang, J. Wang, Z. Guo, Enhanced photocatalytic degradation of norfloxacin in aqueous Bi_2WO_6 dispersions containing nonionic surfactant under visible light irradiation, J. Hazard. Mater. 306 (2016) 295–304, https://doi.org/10.1016/j.jhazmat.2015.12.044.
[11] S. Bhatt, S. Chatterjee, Fluoroquinolone antibiotics: Occurrence, mode of action, resistance, environmental detection, and remediation – A comprehensive review, Environ. Pollut. 315 (2022) 120440, https://doi.org/10.1016/j.envpol.2022.120440.
[12] X. Van Doorslaer, J. Dewulf, H. Van Langenhove, K. Demeestere, Fluoroquinolone antibiotics: An emerging class of environmental micropollutants, Sci. Total Environ. 500–501 (2014) 250–269, https://doi.org/10.1016/j.scitotenv.2014.08.075.
[13] M. Patel, R. Kumar, K. Kishor, T. Mlsna, C.U. Pittman, D. Mohan, Pharmaceuticals of Emerging Concern in Aquatic Systems: Chemistry, Occurrence, Effects, and Removal Methods, Chem. Rev. 119 (2019) 3510–3673, https://doi.org/10.1021/acs.chemrev.8b00299.
[14] Y. Li, Z. Wang, Z. Zou, P. Yu, E. Zhao, H. Zou, J. Wu, Mn-Co/γ-Al_2O_3 coupled with peroxymonosulfate as efficient catalytic system for degradation of norfloxacin, Sep. Purif. Technol. 302 (2022) 122132, https://doi.org/10.1016/j.seppur.2022.122132.
[15] R.D.C. Soltani, M. Mashayekhi, M. Naderi, G. Boczkaj, S. Jorfi, M. Safari, Sonocatalytic degradation of tetracycline antibiotic using zinc oxide nanostructures loaded on nano-cellulose from waste straw as nanosonocatalyst, Ultrason. Sonochem. 55 (2019) 117–124, https://doi.org/10.1016/j.ultsonch.2019.03.009.
[16] T. Narenuch, T. Senasu, T. Chankhanittha, S. Nanan, Solvothermal synthesis of CTAB capped and SDS capped BiOCl photocatalysts for degradation of rhodamine B (RhB) dye and fluoroquinolone antibiotics, J. Solid State Chem. 294 (2021) 121824, https://doi.org/10.1016/j.jssc.2020.121824.
[17] V. Kumar, M. Bilal, L.F.R. Ferreira, Editorial: Recent Trends in Integrated Wastewater Treatment for Sustainable Development, Front. Microbiol. 13 (2022) 846503, https://doi.org/10.3389/fmicb.2022.846503.
[18] H. Ghazal, E. Koumaki, J. Hoslett, S. Malamis, E. Katsou, D. Barcelo, H. Jouhara, Insights into current physical, chemical and hybrid technologies used for the treatment of wastewater contaminated with pharmaceuticals, J. Clean. Prod. 361 (2022) 132079, https://doi.org/10.1016/j.jclepro.2022.132079.
[19] D. Kanakaraju, B.D. Glass, M. Oelgemöller, Advanced oxidation process-mediated removal of pharmaceuticals from water: A review, J. Environ. Manage. 219 (2018) 189–207, https://doi.org/10.1016/j.jenvman.2018.04.103.
[20] H. Sun, F. Guo, J. Pan, W. Huang, K. Wang, W. Shi, One-pot thermal polymerization route to prepare N-deficient modified g-C_3N_4 for the degradation of tetracycline by the synergistic effect of photocatalysis and persulfate-based advanced oxidation process, Chem. Eng. J. 406 (2021) 126844, https://doi.org/10.1016/j.cej.2020.126844.
[21] G. Ren, H. Han, Y. Wang, S. Liu, J. Zhao, X. Meng, Z. Li, Recent Advances of Photocatalytic Application in Water Treatment: A Review, Nanomaterials 11 (2021) 1804, https://doi.org/10.3390/nano11071804.
[22] T.O. Ajiboye, L. Sawunyama, M.P. Ravele, A.A. Rasheed-Adeleke, N.H. Seheri, D.C. Onwudiwe, S.D. Mhlanga, Synthesis approaches to ceramic membranes, their composites, and application in the removal of tetracycline from water, Environ. Adv. 12 (2023) 100371, https://doi.org/10.1016/j.envadv.2023.100371.
[23] S.-L. Zhou, S. Zhang, F. Liu, J.-J. Liu, J.-J. Xue, D.-J. Yang, C.-T. Chang, ZnO nanoflowers photocatalysis of norfloxacin: Effect of triangular silver nanoplates and water matrix on degradation rates, J. Photochem. Photobiol. A Chem. 328 (2016) 97–104, https://doi.org/10.1016/j.jphotochem.2016.03.037.
[24] O. Makota, H.B. Yankovych, O. Bondarchuk, I. Saldan, I. Melnyk, Sphere-shaped ZnO photocatalyst synthesis for enhanced degradation of the Quinolone antibiotic, Ofloxacin, under UV irradiation, Environ. Sci. Pollut. Res. (2024), https://doi.org/10.1007/s11356-024-33619-w.
[25] E. Topkaya, M. Konyar, H.C. Yatmaz, K. Öztürk, Pure ZnO and composite ZnO/TiO_2 catalyst plates: A comparative study for the degradation of azo dye, pesticide and antibiotic in aqueous solutions, J. Colloid Interface Sci. 430 (2014) 6–11, https://doi.org/10.1016/j.jcis.2014.05.022.
[26] Q. Chen, Y. Hao, Z. Song, M. Liu, D. Chen, B. Zhu, J. Chen, Z. Chen, Optimization of photocatalytic degradation conditions and toxicity assessment of norfloxacin under visible light by new lamellar structure magnetic ZnO/g-C_3N_4, Ecotoxicol. Environ. Saf. 225 (2021) 112742, https://doi.org/10.1016/j.ecoenv.2021.112742.
[27] M.G. Batterjee, A. Nabi, M.R. Kamli, K.A. Alzahrani, E.Y. Danish, M.A. Malik,

Green Hydrothermal Synthesis of Zinc Oxide Nanoparticles for UV-Light-Induced Photocatalytic Degradation of Ciprofloxacin Antibiotic in an Aqueous Environment, Catalysts 12 (2022) 1347, https://doi.org/10.3390/catal12111347.
[28] W. Liu, T. He, Y. Wang, G. Ning, Z. Xu, X. Chen, X. Hu, Y. Wu, Y. Zhao, Synergistic adsorption-photocatalytic degradation effect and norfloxacin mechanism of ZnO/ZnS@BC under UV-light irradiation, Sci. Rep. 10 (2020) 11903, https://doi.org/10.1038/s41598-020-68517-x.
[29] T. Chankhanittha, J. Watcharakitti, V. Piyavarakorn, B. Johnson, R.J. Bushby, C. Chuaicham, K. Sasaki, S. Nijpanich, H. Nakajima, N. Chanlek, S. Nanan, ZnO/ZnS photocatalyst from thermal treatment of ZnS: Influence of calcination temperature on development of heterojunction structure and photocatalytic performance, J. Phys. Chem. Solids 179 (2023) 111393, https://doi.org/10.1016/j.jpcs.2023.111393.
[30] A.E.B. Lima, R.Y.N. Reis, L.S. Ribeiro, L.K. Ribeiro, M. Assis, R.S. Santos, C.H.M. Fernandes, L.S. Cavalcante, E. Longo, J.A.O. Osajima, G.E. Luz, Microwave-assisted hydrothermal synthesis of $CuWO_4$-palygorskite nanocomposite for enhanced visible photocatalytic response, J. Alloys Compd. 863 (2021) 158731, https://doi.org/10.1016/j.jallcom.2021.158731.
[31] K. Sahu, A.K. Kar, Counterion-Induced Tailoring of Energy Transfer in Hydrothermally Grown Nanostructured ZnO for Photocatalysis, Cryst. Growth Des. 21 (2021) 3656–3667, https://doi.org/10.1021/acs.cgd.0c01202.
[32] M. Pudukudy, Z. Yaakob, Simple chemical synthesis of novel ZnO nanostructures: Role of counter ions, Solid State Sci. 30 (2014) 78–88, https://doi.org/10.1016/j.solidstatesciences.2014.02.008.
[33] M.S. Khan, P.P. Dhavan, D. Ratna, N.G. Shimpi, Ultrasonic-assisted biosynthesis of ZnO nanoparticles using Sonneratia alba leaf extract and investigation of its photocatalytic and biological activities, J. Clust. Sci. 33 (2022) 1007–1023, https://doi.org/10.1007/s10876-021-02036-1.
[34] K. Yu, J. Shi, Z. Zhang, Y. Liang, W. Liu, Synthesis, Characterization, and Photocatalysis of ZnO and Er-Doped ZnO, J. Nanomater. 2013 (2013) 372951, https://doi.org/10.1155/2013/372951.
[35] J. Liu, X. Huang, K.M. Sulieman, F. Sun, X. He, Solution-Based Growth and Optical Properties of Self-Assembled Monocrystalline ZnO Ellipsoids, J. Phys. Chem. B 110 (2006) 10612–10618, https://doi.org/10.1021/jp056880r.
[36] A.C. Catto, M.M. Ferrer, O.F. Lopes, V.R. Mastelaro, J. Andrés, L.F. da Silva, E. Longo, W. Avansi, The role of counter-ions in crystal morphology, surface structure and photocatalytic activity of ZnO crystals grown onto a substrate, Appl. Surf. Sci. 529 (2020) 147057, https://doi.org/10.1016/j.apsusc.2020.147057.
[37] X.-G. Han, Y.-Q. Jiang, S.-F. Xie, Q. Kuang, X. Zhou, D.-P. Cai, Z.-X. Xie, L.-S. Zheng, Control of the Surface of ZnO Nanostructures by Selective Wet-Chemical Etching, J. Phys. Chem. C 114 (2010) 10114–10118, https://doi.org/10.1021/jp101284p.
[38] E.S. Jang, J.-H. Won, S.-J. Hwang, J.-H. Choy, Fine Tuning of the Face Orientation of ZnO Crystals to Optimize Their Photocatalytic Activity, Adv. Mater. 18 (2006) 3309–3312, https://doi.org/10.1002/adma.200601455.
[39] X. Pan, M.-Q. Yang, Y.-J. Xu, Morphology control, defect engineering and photoactivity tuning of ZnO crystals by graphene oxide – a unique 2D macromolecular surfactant, Phys. Chem. Chem. Phys. 16 (2014) 5589–5599, https://doi.org/10.1039/c3cp55038a.
[40] X. Qin, D. Shi, B. Guo, C. Fu, J. Zhang, Q. Xie, X. Shi, F. Chen, X. Qin, W. Yu, X. Feng, Y. Liu, D. Luo, Anion-Regulated Synthesis of ZnO 1D Necklace-Like Nanostructures with High Photocatalytic Activity, Nanoscale Res. Lett. 15 (2020) 206, https://doi.org/10.1186/s11671-020-03435-5.
[41] R.C. Pawar, H. Kim, C.S. Lee, Defect-controlled growth of ZnO nanostructures using its different zinc precursors and their application for effective photodegradation, Curr. Appl. Phys. 14 (2014) 621–629, https://doi.org/10.1016/j.cap.2014.02.003.
[42] R.C. Pawar, J.S. Shaikh, S.S. Suryavanshi, P.S. Patil, Growth of ZnO nanodisk, nanospindles and nanoflowers for gas sensor: pH dependency, Curr. Appl. Phys. 12 (2012) 778–783, https://doi.org/10.1016/j.cap.2011.11.005.
[43] G.P. Barreto, G. Morales, M.L.L. Quintanilla, Microwave Assisted Synthesis of ZnO Nanoparticles: Effect of Precursor Reagents, Temperature, Irradiation Time, and Additives on Nano-ZnO Morphology Development, J. Mater. 2013 (2013) 478681, https://doi.org/10.1155/2013/478681.
[44] C.A. Zito, T.M. Perfecto, T.N.T. Oliveira, D.P. Volanti, Bicone-like ZnO structure as high-performance butanone sensor, Mater. Lett. 223 (2018) 142–145, https://doi.org/10.1016/j.matlet.2018.04.026.
[45] A.P.A. Oliveira, J.-F. Hochepied, F. Grillon, M.-H. Berger, Controlled Precipitation of Zinc Oxide Particles at Room Temperature, Chem. Mater. 15 (2003) 3202–3207, https://doi.org/10.1021/cm0213725.
[46] X. Pu, D. Zhang, X. Yi, X. Shao, W. Li, M. Sun, L. Li, X. Qian, Rapid chemical synthesis and optical properties of ZnO ellipsoidal nanostructures, Adv. Powder Technol. 21 (2010) 344–349, https://doi.org/10.1016/j.apt.2010.02.010.
[47] M.C. Uribe-López, M.C. Hidalgo-López, R. López-González, D.M. Frías-Márquez, G. Núñez-Nogueira, D. Hernández-Castillo, M.A. Alvarez-Lemus, Photocatalytic activity of ZnO nanoparticles and the role of the synthesis method on their physical and chemical properties, J. Photochem. Photobiol. A Chem. 404 (2021) 112866, https://doi.org/10.1016/j.jphotochem.2020.112866.
[48] M. Prabhu, J. Mayandi, R.N. Mariammal, V. Vishnukanthan, J.M. Pearce, N. Soundararajan, K. Ramachandran, Peanut shaped ZnO microstructures: controlled synthesis and nucleation growth toward low-cost dye sensitized solar cells, Mater. Res. Express 2 (2015) 66202, https://doi.org/10.1088/2053-1591/2/6/066202.
[49] S. Rajamanickam, S.M. Mohammad, Z. Hassan, Effect of zinc acetate dihydrate concentration on morphology of ZnO seed layer and ZnO nanorods grown by hydrothermal method, Colloid Interface Sci. Commun. 38 (2020) 100312, https://doi.org/10.1016/j.colcom.2020.100312.
[50] M.K. Kavitha, K.B. Jinesh, R. Philip, P. Gopinath, H. John, Defect engineering in ZnO nanocones for visible photoconductivity and nonlinear absorption, Phys. Chem. Chem. Phys. 16 (2014) 25093–25100, https://doi.org/10.1039/C4CP03847A.
[51] S. Dey, S. Das, A.K. Kar, Role of precursor dependent nanostructures of ZnO on its optical and photocatalytic activity and influence of FRET between ZnO and methylene blue dye on photocatalysis, Mater. Chem. Phys. 270 (2021) 124872, https://doi.org/10.1016/j.matchemphys.2021.124872.
[52] S. Agarwal, L.K. Jangir, K.S. Rathore, M. Kumar, K. Awasthi, Morphology-dependent structural and optical properties of ZnO nanostructures, Appl. Phys. A 125 (2019) 553, https://doi.org/10.1007/s00339-019-2852-x.
[53] T. Vu Anh, T.A.T. Pham, V.H. Mac, T.H. Nguyen, Facile Controlling of the Physical Properties of Zinc Oxide and Its Application to Enhanced Photocatalysis, J. Anal. Methods Chem. (2021 (2021)) 5533734, https://doi.org/10.1155/2021/5533734.
[54] V.K. Jayaraman, A. Hernández-Gordillo, M. Bizarro, Importance of precursor type in fabricating ZnO thin films for photocatalytic applications, Mater. Sci. Semicond. Process. 75 (2018) 36–42, https://doi.org/10.1016/j.mssp.2017.11.015.
[55] V.V. Kadam, S.D. Shanmugam, J.P. Ettiyappan, R.M. Balakrishnan, Photocatalytic degradation of p-nitrophenol using biologically synthesized ZnO nanoparticles, Environ. Sci. Pollut. Res. 28 (2021) 12119–12130, https://doi.org/10.1007/s11356-020-10833-w.
[56] Y. Sun, L. Chen, Y. Bao, Y. Zhang, J. Wang, M. Fu, J. Wu, D. Ye, The Applications of Morphology Controlled ZnO in Catalysis, Catalysts 6 (2016) 188, https://doi.org/10.3390/catal6120188.
[57] M. Cai, A. Shui, B. Du, Constructing the ZnO/BiOBr hierarchical heterojunction for efficient pollutant photodegradation driven by visible-light, Surfaces and Interfaces 37 (2023) 102643, https://doi.org/10.1016/j.surfin.2023.102643.
[58] M.P. Ramike, P.G. Ndungu, M.A. Mamo, Exploration of the Different Dimensions of Wurtzite ZnO Structure Nanomaterials as Gas Sensors at Room Temperature, Nanomaterials 13 (2023) 2810, https://doi.org/10.3390/nano13202810.
[59] S.U. Awan, S.K. Hasanain, J. Rashid, S. Hussain, S.A. Shah, M.Z. Hussain, M. Rafique, M. Aftab, R. Khan, Structural, optical, electronic and magnetic properties of multiphase ZnO/$Zn(OH)_2$/ZnO_2 nanocomposites and hexagonal prism shaped ZnO nanoparticles synthesized by pulse laser ablation in Heptanes, Mater. Chem. Phys. 211 (2018) 510–521, https://doi.org/10.1016/j.matchemphys.2018.02.051.
[60] X. He, Y. Yang, Y. Li, J. Chen, S. Yang, R. Liu, Z. Xu, Effects of structure and surface properties on the performance of ZnO towards photocatalytic degradation of methylene blue, Appl. Surf. Sci. 599 (2022) 153898, https://doi.org/10.1016/j.apsusc.2022.153898.
[61] T.K. Le, T.M.T. Nguyen, H.T.P. Nguyen, T.K.L. Nguyen, T. Lund, H.K.H. Nguyen, T.K.X. Huynh, Enhanced photocatalytic activity of ZnO nanoparticles by surface modification with KF using thermal shock method, Arab. J. Chem. 13 (2020) 1032–1039, https://doi.org/10.1016/j.arabjc.2017.09.006.
[62] B. Sanches de Lima, P.R. Martínez-Alanis, F. Güell, W.A. dos Santos Silva, M.I.B. Bernardi, N.L. Marana, E. Longo, J.R. Sambrano, V.R. Mastelaro, Experimental and Theoretical Insights into the Structural Disorder and Gas Sensing Properties of ZnO, ACS Appl. Electron. Mater. 3 (2021) 1447–1457, https://doi.org/10.1021/acsaelm.1c00058.
[63] G.T.S.T. da Silva, K.T.G. Carvalho, O.F. Lopes, E.S. Gomes, A.R. Malagutti, V.R. Mastelaro, C. Ribeiro, H.A.J.L. Mourão, Synthesis of ZnO Nanoparticles Assisted by N Sources and their Application in the Photodegradation of Organic Contaminants, ChemCatChem 9 (2017) 3795–3804, https://doi.org/10.1002/cctc.201700756.
[64] J. Patel, A.K. Singh, S.A.C. Carabineiro, Assessing the Photocatalytic Degradation of Fluoroquinolone Norfloxacin by Mn:ZnS Quantum Dots: Kinetic Study, Degradation Pathway and Influencing Factors, Nanomaterials 10 (2020) 964, https://doi.org/10.3390/nano10050964.
[65] S. Han, J. Ren, Y. Sun, H. Li, X. Zhang, Ternary CuO/ZnO/g-C_3N_4 Composite for Enhanced UV-Light Photocatalytic Degradation of Norfloxacin, SSRN Electron. J. (2022), https://doi.org/10.2139/ssrn.4258694.
[66] A.F. A, S. Narayanan, BAGSPl of mesoporous Ag/ZnO nanostructures for visible light mediated photocatalytic removal of ciprofloxacin from water; a morphological perspective, Inorg. Chem. Commun. 154 (2023) 110966, https://doi.org/10.1016/j.inoche.2023.110966.
[67] S. Das, S. Ghosh, A. Misra, A. Tamhankar, A. Mishra, C. Lundborg, S. Tripathy, Sunlight Assisted Photocatalytic Degradation of Ciprofloxacin in Water Using Fe Doped ZnO Nanoparticles for Potential Public Health Applications, Int. J. Environ. Res. Public Health 15 (2018) 2440, https://doi.org/10.3390/ijerph15112440.
[68] S.-B. Hu, L. Li, M.-Y. Luo, Y.-F. Yun, C.-T. Chang, Aqueous norfloxacin sonocatalytic degradation with multilayer flower-like ZnO in the presence of peroxydisulfate, Ultrason. Sonochem. 38 (2017) 446–454, https://doi.org/10.1016/j.ultsonch.2017.03.044.
[69] C. Feng, Y. Wang, Z. Lu, Q. Liang, Y. Zhang, Z. Li, S. Xu, Nanoflower Ni_5P_4 coupled with GCNQDs as Schottky junction photocatalyst for the efficient degradation of norfloxacin, Sep. Purif. Technol. 282 (2022) 120107, https://doi.org/10.1016/j.seppur.2021.120107.
[70] J. Lei, B. Chen, L. Zhou, N. Ding, Z. Cai, L. Wang, S.-I. In, C. Cui, Y. Zhou, Y. Liu, J. Zhang, Efficient degradation of antibiotics in different water matrices through the photocatalysis of inverse opal K-g-C_3N_4: Insights into mechanism and assessment of antibacterial activity, Chem. Eng. J. 400 (2020) 125902, https://doi.org/10.1016/j.cej.2020.125902.

[71] B. Shao, X. Liu, Z. Liu, G. Zeng, Q. Liang, C. Liang, Y. Cheng, W. Zhang, Y. Liu, S. Gong, A novel double Z-scheme photocatalyst $Ag_3PO_4/Bi_2S_3/Bi_2O_3$ with enhanced visible-light photocatalytic performance for antibiotic degradation, Chem. Eng. J. 368 (2019) 730–745, https://doi.org/10.1016/j.cej.2019.03.013.

[72] L. Li, C.-G. Niu, H. Guo, J. Wang, M. Ruan, L. Zhang, C. Liang, H.-Y. Liu, Y.-Y. Yang, Efficient degradation of Levofloxacin with magnetically separable $ZnFe_2O_4$/NCDs/Ag_2CO_3 Z-scheme heterojunction photocatalyst: Vis-NIR light response ability and mechanism insight, Chem. Eng. J. 383 (2020) 123192, https://doi.org/10.1016/j.cej.2019.123192.

[73] Z.-H. Diao, S.-T. Huang, X. Chen, M.-Y. Zou, H. Liu, P.-R. Guo, L.-J. Kong, W. Chu, Peroxymonosulfate-assisted photocatalytic degradation of antibiotic norfloxacin by a calcium-based Ag_3PO_4 composite in water: Reactivity, products and mechanism, in, J. Clean. Prod. 330 (2022) 129806, https://doi.org/10.1016/j.jclepro.2021.129806.

[74] T.T. Dao, T. Le Na Vo, A.T. Duong, D.T. Tran, D.L. Nguyen, V.V. Pham, R. Das, H.T. Nguyen, Highly photocatalytic activity of pH-controlled ZnO nanoflakes, Opt. Mater. (amst). 140 (2023) 113865, https://doi.org/10.1016/j.optmat.2023.113865.

[75] G. Zhang, Y. Xue, Q. Wang, P. Wang, H. Yao, W. Zhang, J. Zhao, Y. Li, Photocatalytic oxidation of norfloxacin by $Zn_{0.9}Fe_{0.1}S$ supported on Ni-foam under visible light irradiation, Chemosphere 230 (2019) 406–415, https://doi.org/10.1016/j.chemosphere.2019.05.015.

[76] N. Tahir, M. Zahid, I.A. Bhatti, Y. Jamil, Fabrication of visible light active Mn-doped Bi_2WO_6-GO/MoS_2 heterostructure for enhanced photocatalytic degradation of methylene blue, Environ. Sci. Pollut. Res. 29 (2022) 6552–6567, https://doi.org/10.1007/s11356-021-16094-5.

[77] C. Zhang, M. Jia, Z. Xu, W. Xiong, Z. Yang, J. Cao, H. Peng, H. Xu, Y. Xiang, Y. Jing, Constructing 2D/2D N-ZnO/g-C_3N_4 S-scheme heterojunction: Efficient photocatalytic performance for norfloxacin degradation, Chem. Eng. J. 430 (2022) 132652, https://doi.org/10.1016/j.cej.2021.132652.

[78] M. Manasa, P.R. Chandewar, H. Mahalingam, Photocatalytic degradation of ciprofloxacin & norfloxacin and disinfection studies under solar light using boron & cerium doped TiO_2 catalysts synthesized by green EDTA-citrate method, Catal. Today 375 (2021) 522–536, https://doi.org/10.1016/j.cattod.2020.03.018.

[79] G.N. Marques, A.J. Moreira, E.T.D. Nóbrega, S. Braga, M.N. Argentin, I.L.B. da Cunha Camargo, E. Azevedo, E.C. Pereira, M.I.B. Bernardi, L.H. Mascaro, Selective inhibitory activity of multidrug-resistant bacteria by zinc oxide nanoparticles, J. Environ Chem. Eng. 12 (2024) 111870, https://doi.org/10.1016/j.jece.2023.111870.

[80] Y. Núñez-de la Rosa, L.G.C. Durango, M.R. Forim, O.R. Nascimento, P. Hammer, J.M. Aquino, Unraveling the time evolution and post mortem changes of nanometric MnOOH during in situ oxidation of ciprofloxacin by activated peroxymonosulfate, Appl. Catal. B Environ. 327 (2023) 122439, https://doi.org/10.1016/j.apcatb.2023.122439.

[81] J.M. Fontmorin, R.C. Burgos Castillo, W.Z. Tang, M. Sillanpää, Stability of 5,5-dimethyl-1-pyrroline-N-oxide as a spin-trap for quantification of hydroxyl radicals in processes based on Fenton reaction, Water Res. 99 (2016) 24–32, https://doi.org/10.1016/j.watres.2016.04.053.

[82] J. Luan, L. Hao, Y. Yao, Y. Wang, G. Yang, J. Li, Synthesis, Characterization of Dy_2NdSbO_7/Bi_2WO_6 Heterojunction Photocatalyst and the Application for the Photocatalytic Degradation of Chlorpyrifos under Visible Light Irradiation, Crystals 14 (2023) 55, https://doi.org/10.3390/cryst14010055.

[83] M.H.A. Feitosa, A.M. Santos, A. Wong, C.A.F. Moraes, G.M. Grosseli, O.R. Nascimento, P.S. Fadini, F.C. Moraes, Photoelectrocatalytic removal of antibiotic ciprofloxacin using a photoanode based on Z-scheme heterojunction, Chem. Eng. J. 493 (2024) 152291, https://doi.org/10.1016/j.cej.2024.152291.

[84] F. Collin, Chemical Basis of Reactive Oxygen Species Reactivity and Involvement in Neurodegenerative Diseases, Int. J. Mol. Sci. 20 (2019) 2407, https://doi.org/10.3390/ijms20102407.

[85] A. Lipovsky, Z. Tzitrinovich, H. Friedmann, G. Applerot, A. Gedanken, R. Lubart, EPR Study of Visible Light-Induced ROS Generation by Nanoparticles of ZnO, J. Phys. Chem. C 113 (2009) 15997–16001, https://doi.org/10.1021/jp904864g.

[86] E. Finkelstein, G.M. Rosen, E.J. Rauckman, Spin trapping of superoxide and hydroxyl radical: Practical aspects, Arch. Biochem. Biophys. 200 (1980) 1–16, https://doi.org/10.1016/0003-9861(80)90323-9.

[87] L. Zhang, Y. Nie, C. Hu, J. Qu, Enhanced Fenton degradation of Rhodamine B over nanoscaled Cu-doped $LaTiO_3$ perovskite, Appl. Catal. B Environ. 125 (2012) 418–424, https://doi.org/10.1016/j.apcatb.2012.06.015.

[88] D.G. Ayu, S. Gea, D.J. Andriayani, A.F.R. Telaumbanua, M. Piliang, Z. Harahap, R. Yen, A.I.Y.T. Goei, Photocatalytic Degradation of Methylene Blue Using N-Doped ZnO/Carbon Dot (N-ZnO/CD) Nanocomposites Derived from Organic Soybean, ACS Omega 8 (2023) 14965–14984, https://doi.org/10.1021/acsomega.2c07546.

[89] G. Su, T. Feng, Z. Huang, Y. Zheng, W. Zhang, G. Liu, W. Wang, H. Wei, L. Dang, MOF derived hollow CuO/ZnO nanocages for the efficient and rapid degradation of fluoroquinolones under natural sunlight, Chem. Eng. J. 436 (2022) 135119, https://doi.org/10.1016/j.cej.2022.135119.

[90] I. Sánchez-Montes, G.O.S. Santos, T.O. Silva, R. Colombo, M.R.V. Lanza, An innovative approach to the application of electrochemical processes based on the in-situ generation of H_2O_2 for water treatment, J. Clean. Prod. 392 (2023) 136242, https://doi.org/10.1016/j.jclepro.2023.136242.

[91] D. Ding, C. Liu, Y. Ji, Q. Yang, L. Chen, C. Jiang, T. Cai, Mechanism insight of degradation of norfloxacin by magnetite nanoparticles activated persulfate: Identification of radicals and degradation pathway, Chem. Eng. J. 308 (2017) 330–339, https://doi.org/10.1016/j.cej.2016.09.077.

[92] J.F. Carneiro, J.M. Aquino, B.F. Silva, A.J. Silva, R.C. Rocha-Filho, Comparing the electrochemical degradation of the fluoroquinolone antibiotics norfloxacin and ciprofloxacin using distinct electrolytes and a BDD anode: evolution of main oxidation byproducts and toxicity, J. Environ. Chem. Eng. 8 (2020) 104433, https://doi.org/10.1016/j.jece.2020.104433.

[93] C. Liu, V. Nanaboina, G.V. Korshin, W. Jiang, Spectroscopic study of degradation products of ciprofloxacin, norfloxacin and lomefloxacin formed in ozonated wastewater, Water Res. 46 (2012) 5235–5246, https://doi.org/10.1016/j.watres.2012.07.005.

[94] D.A.C. Coledam, J.M. Aquino, B.F. Silva, A.J. Silva, R.C. Rocha-Filho, Electrochemical mineralization of norfloxacin using distinct boron-doped diamond anodes in a filter-press reactor, with investigations of toxicity and oxidation by-products, Electrochim. Acta 213 (2016) 856–864, https://doi.org/10.1016/j.electacta.2016.08.003.

[95] S. Babić, M. Periša, I. Škorić, Photolytic degradation of norfloxacin, enrofloxacin and ciprofloxacin in various aqueous media, Chemosphere 91 (2013) 1635–1642, https://doi.org/10.1016/j.chemosphere.2012.12.072.

[96] J. Arshad, N.K. Janjua, R. Raza, Synthesis of Novel (Be, Mg, Ca, Sr, Zn_{Ni})3O4 High Entropy Oxide with Characterization of Structural and Functional Properties and Electrochemical Applications, J. Electrochem. Sci. Technol. 12 (2021) 112–125. https://doi.org/10.33961/jecst.2020.01130.

[97] X. Zhang, G. Chen, W. Li, D. Wu, Preparation and Photocathodic Protection Properties of ZnO/TiO_2 Heterojunction Film Under Simulated Solar Light, Materials (basel). 12 (2019) 3856, https://doi.org/10.3390/ma12233856.

[98] T. Jan, S. Raheem, S.V. Sawant, T.V. Manolikar, S.S. Sakate, S.K. Pardeshi, R.M. Jagtap, M.A. Rizvi, Photocatalytic evaluation of CuO and ZnO crystallites synthesized hydrothermally using binary eugenol/iso-eugenol mixtures: isomer effects on the capping propensity of biogenic agents, New J. Chem. 48 (2024) 5040–5059, https://doi.org/10.1039/D3NJ05237K.

[99] F. Bouhjar, B. Marí, B. Bessaïs, Hydrothermal fabrication and characterization of ZnO/Fe_2O_3 heterojunction devices for hydrogen production, J. Anal. Pharm. Res. 7 (2018) 315–321. https://doi.org/10.15406/japlr.2018.07.00246.

[100] S.S. Patil, M.G. Mali, M.S. Tamboli, D.R. Patil, M.V. Kulkarni, H. Yoon, H. Kim, S.S. Al-Deyab, S.S. Yoon, S.S. Kolekar, B.B. Kale, Green approach for hierarchical nanostructured Ag-ZnO and their photocatalytic performance under sunlight, Catal. Today 260 (2016) 126–134, https://doi.org/10.1016/j.cattod.2015.06.004.

[101] A.B. Djurišić, Y.H. Leung, K.H. Tam, Y.F. Hsu, L. Ding, W.K. Ge, Y.C. Zhong, K.S. Wong, W.K. Chan, H.L. Tam, K.W. Cheah, W.M. Kwok, D.L. Phillips, Defect emissions in ZnO nanostructures, Nanotechnology 18 (2007) 95702, https://doi.org/10.1088/0957-4484/18/9/095702.

[102] M.S. Rathore, H. Verma, S.B. Akhani, J. Pathak, U. Joshi, A. Joshi, C. Prakash, K. Kaur, A. Oza, Photoluminescence and antibacterial performance of sol–gel synthesized ZnO nanoparticles, Mater. Adv. 5 (2024) 3472–3481, https://doi.org/10.1039/D3MA01096A.

[103] L. Kumar Jangir, Y. Kumari, A. Kumar, M. Kumar, K. Awasthi, Investigation of luminescence and structural properties of ZnO nanoparticles, synthesized with different precursors, Mater. Chem. Front. 1 (2017) 1413–1421, https://doi.org/10.1039/C7QM00058H.

[104] R.B.M. Cross, M.M. De Souza, E.M.S. Narayanan, A low temperature combination method for the production of ZnO nanowires, Nanotechnology 16 (2005) 2188–2192, https://doi.org/10.1088/0957-4484/16/10/035.

[105] X. Zhu, J. Wang, D. Yang, J. Liu, L. He, M. Tang, W. Feng, X. Wu, Fabrication, characterization and high photocatalytic activity of Ag–ZnO heterojunctions under UV-visible light, RSC Adv. 11 (2021) 27257–27266, https://doi.org/10.1039/D1RA05060E.

[106] L. Saikia, D. Bhuyan, M. Saikia, B. Malakar, D.K. Dutta, P. Sengupta, Photocatalytic performance of ZnO nanomaterials for self sensitized degradation of malachite green dye under solar light, Appl. Catal. A Gen. 490 (2015) 42–49, https://doi.org/10.1016/j.apcata.2014.10.053.

[107] T. Mahardika, N.A. Putri, A.E. Putri, V. Fauzia, L. Roza, I. Sugihartono, Y. Herbani, Rapid and low temperature synthesis of Ag nanoparticles on the ZnO nanorods for photocatalytic activity improvement, Results Phys. 13 (2019) 102209, https://doi.org/10.1016/j.rinp.2019.102209.

[108] H. Chen, W. Liu, Z. Qin, ZnO/$ZnFe_2O_4$ nanocomposite as a broad-spectrum photo-Fenton-like photocatalyst with near-infrared activity, Catal, Sci. Technol. 7 (2017) 2236–2244, https://doi.org/10.1039/C7CY00308K.

[109] V. Kumar, S. Choudhary, V. Malik, R. Nagarajan, A. Kandasami, A. Subramanian, Enhancement in Photocatalytic Activity of $SrTiO_3$ by Tailoring Particle Size and Defects, Phys. Status Solidi 216 (2019) 1900294, https://doi.org/10.1002/pssa.201900294.

[110] X. Wang, C. Guo, X. Hu, Y. Xu, C. Zhang, J. Wei, J. Weng, Y. Liu, L. Fu, Q. Wang, T. Yang, Self-assembled oxygen vacancies modified hierarchical hollow tubular Bi_2WO_6/In_2O_3 Z-scheme heterojunction for optimized photocatalytic degradation of norfloxacin, J. Environ. Chem. Eng. 12 (2024) 112010, https://doi.org/10.1016/j.jece.2024.112010.

[111] H. Tan, Z. Zhao, W. Zhu, E.N. Coker, B. Li, M. Zheng, W. Yu, H. Fan, Z. Sun, Oxygen Vacancy Enhanced Photocatalytic Activity of Pervoskite $SrTiO_3$, ACS Appl. Mater. Interfaces 6 (2014) 19184–19190, https://doi.org/10.1021/am5051907.

[112] A. Sengar, A. Vijayanandan, Human health and ecological risk assessment of 98 pharmaceuticals and personal care products (PPCPs) detected in Indian surface and wastewaters, Sci. Total Environ. 807 (2022) 150677, https://doi.org/10.1016/j.scitotenv.2021.150677.

[113] M. Gholami, H. Rasoulzadeh, T. Ahmadi, M. Hosseini, Synthesis, characterization of Nickel doped Zinc oxide by radio-frequency sputtering and

application in photo-electrocatalysis degradation of Norfloxacin, Mater. Lett. 269 (2020) 127647, https://doi.org/10.1016/j.matlet.2020.127647.
[114] L.-F. Tian, Y.-Z. Hu, Y.-R. Guo, Q.-J. Pan, Dual effect of lignin amine on fabrication of magnetic Fe_3O_4/C/ZnO nanocomposite in situ and photocatalytic property, Ceram. Int. 44 (2018) 14480–14486, https://doi.org/10.1016/j.ceramint.2018.05.062.
[115] G. Shankaraiah, S. Poodari, D. Bhagawan, V. Himabindu, S. Vidyavathi, Degradation of antibiotic norfloxacin in aqueous solution using advanced oxidation processes (AOPs)—A comparative study, Desalin. Water Treat. 57 (2016) 27804–27815, https://doi.org/10.1080/19443994.2016.1176960.
[116] M. Sayed, L.A. Shah, J.A. Khan, N.S. Shah, J. Nisar, H.M. Khan, P. Zhang, A.R. Khan, Efficient Photocatalytic Degradation of Norfloxacin in Aqueous Media by Hydrothermally Synthesized Immobilized TiO2/Ti Films with Exposed 001 Facets, J. Phys. Chem. A 120 (2016) 9916–9931, https://doi.org/10.1021/acs.jpca.6b09719.
[117] J. Bai, Y. Li, P. Jin, J. Wang, L. Liu, Facile preparation 3D ZnS nanospheres-reduced graphene oxide composites for enhanced photodegradation of norfloxacin, J. Alloys Compd. 729 (2017) 809–815, https://doi.org/10.1016/j.jallcom.2017.07.057.
[118] T. Senasu, T. Narenuch, K. Wannakam, T. Chankhanittha, S. Nanan, Solvothermally grown BiOCl catalyst for photodegradation of cationic dye and fluoroquinolone-based antibiotics, J. Mater. Sci. Mater. Electron. 31 (2020) 9685–9694, https://doi.org/10.1007/s10854-020-03514-4.
[119] D. Song, M. Li, L. Liao, L. Guo, H. Liu, B. Wang, Z. Li, High-Crystallinity BiOCl Nanosheets as Efficient Photocatalysts for Norfloxacin Antibiotic Degradation, Nanomaterials 13 (2023) 1841, https://doi.org/10.3390/nano13121841.